ELSEVIER

J. Non-Newtonian Fluid Mech. 149 (2008) 104–123

Journal of Non-Newtonian Fluid Mechanics

www.elsevier.com/locate/jnnfm

A computational study of the effect of viscoelasticity on slot coating flow of dilute polymer solutions

Mohit Bajaj [a], J. Ravi Prakash [a], Matteo Pasquali [b,*]

[a] Department of Chemical Engineering, Monash University, Clayton, Vic. 3800, Australia
[b] Department of Chemical and Biomolecular Engineering and Computer and Information Technology Institute,
Rice University, MS 362, 6100 Main Street, Houston, TX 77005, USA

Received 2 November 2006; received in revised form 30 April 2007; accepted 19 May 2007

Abstract

We study the effect of viscoelasticity on the fluid dynamics of slot coating flow of dilute polymer solutions. The fluid is modeled by the Oldroyd-B and FENE-P equations in a conformation tensor formulation. The fully coupled equations of the flow are solved by the DEVSS-TG finite element method together with the elliptic domain mapping method to capture the unknown free surface. We observe that dilute solutions, where the presence of polymer molecules affects the flow field, behave qualitatively differently from ultra-dilute solutions, where the presence of polymer molecules does not alter the flow field. In dilute solutions: (1) the stagnation point on the free surface moves towards the static contact line and the recirculation zone shrinks with increasing Weissenberg number; (2) once the stagnation point reaches the static contact line, the hoop stress on the free surface changes sign from negative to positive, which destabilizes the flow; (3) the region of most severe polymer stretch and distortion also moves to the static contact line. The field variables, such as velocity, velocity gradient and conformation tensor, become singular due to a geometric singularity at the static contact line which leads to the failure of the computational method. In contrast, in ultra-dilute solutions, the computations fail when the mesh can not capture steep stress boundary layers at the free surface. The low-flow limit of inertialess slot coating flow is examined in terms of the Elastocapillary number; the coating window for uniform coating narrows as the liquid grows more elastic.

Keywords: Elastic coating; Slot coating; Polymer solutions

1. Introduction

Slot coating belongs to a class of coating flows known as pre-metered coating, where the thickness of the coated layer is predetermined. In pre-metered coating, all the liquid fed into the coating die by a metering device, e.g., a displacement pump, is deposited on the substrate (see Fig. 1). As a result, the average film thickness is predetermined for a given feed flow rate, coating width in the cross-web direction, and substrate speed, and is consequently ideal for high precision coating. The average film thickness is independent of the rheological properties of the coating liquid.

Frequently, coating applications involve liquids that are viscoelastic due to the presence of polymer as a final product or as a rheology modifier. Most of these flows are time dependent and their dynamics are controlled by the elasticity and capillarity of the liquid. The competition among viscous, capillary and elastic forces (also inertial forces if the Reynolds number (*Re*) is sufficiently high) determines the range of parameters in which the flow is stable and steady. Although the coating thickness is independent of the non-Newtonian nature of the liquid, the flow in the coating bead and the uniformity of the liquid layer are affected by the rheological properties of the liquid [1].

Until recently, coating flow research has largely been based on steady Newtonian coating flows [2–12] and their stability [13–18]. Studies related to viscoelastic coating flows have only recently been attempted and are limited [19–25]. For slot coating flow in particular, calculations of steady Newtonian [3,4,9–12] and viscoelastic flows [19,20,23,25] have been reported in the literature. To some extent, the limited number of studies in the area of viscoelastic coating flow can be attributed to the complexity posed by the presence of free surfaces especially at low Capillary number, *Ca* (defined as the ratio of viscous to surface forces). Modeling coating flows requires equations and computational methods which can describe and predict the molecular conformation of polymers in the flow field while

---

* Corresponding author. Tel.: +1 713 348 5830; fax: +1 713 348 5478.
E-mail address: mp@rice.edu (M. Pasquali).

0377-0257/$ – see front matter © 2007 Elsevier B.V. All rights reserved.
doi:10.1016/j.jnnfm.2007.05.013

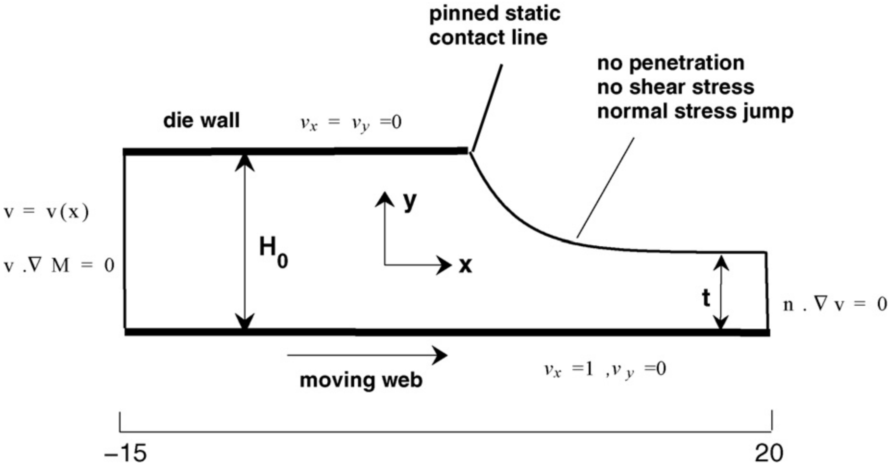

Fig. 1. Flow domain and boundary conditions used in analyzing the flow of viscoelastic liquid in the downstream section of a slot coater.

simultaneously capturing accurately the shape of free surfaces. The location of the free surface is unknown *a priori* and capturing its location is a part of the problem solution. Different ways of handling free surface flows are discussed in detail in Refs. [1,5,26,27].

The work by Pasquali and Scriven [19], Lee et al. [20] and Bajaj et al. [25] highlight the following aspects of viscoelastic slot coating flows.

Pasquali and Scriven [19] carried out flow computations of different coating operations for both the dilute and ultra-dilute solutions using conformation tensor based constitutive models. In *ultra-dilute* solutions conservation equations are decoupled from the conformation tensor equation and as a result, the velocity field is computed independent of the polymer stress. In case of slot coating of ultra-dilute solutions, they observed that the recirculation under the die strongly affects the computations at

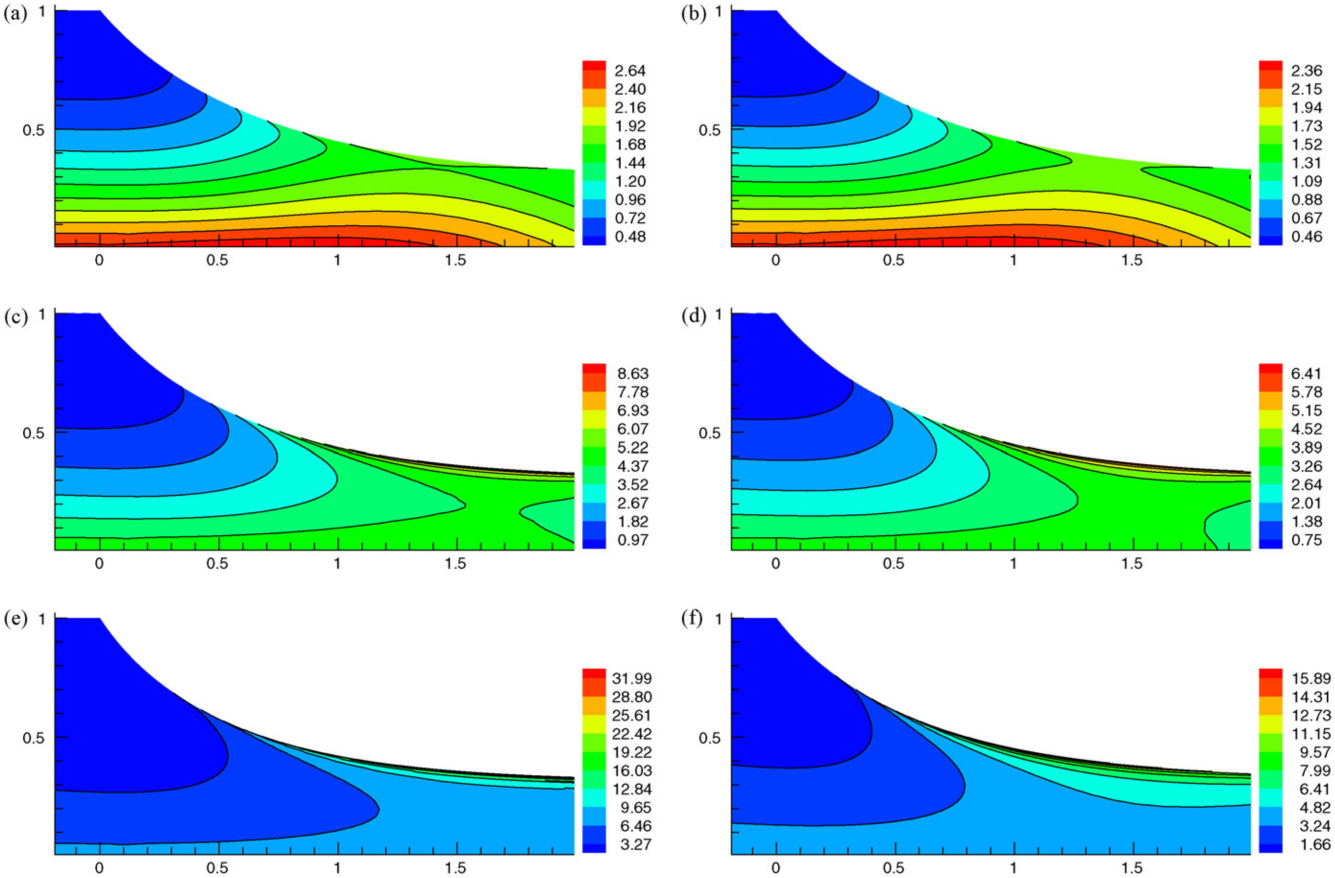

Fig. 2. Evolution of the xx component of the elastic stress (σ_{xx}) as a function of Wi for Oldroyd-B (a, c and e) and FENE-P (b, d and f) models. $Ca = 0.1$, $Q = 0.3$, $\beta = 0.75$, $b = 50$. (a and b) $Wi = 1.0$, (c and d) $Wi = 2.0$ and (e and f) $Wi = 3.0$.

high Weissenberg number *Wi* ($Wi = \lambda\dot{\gamma}$, where λ is the characteristic relaxation time of polymer, and $\dot{\gamma}$ is the characteristic rate of strain). In the absence of recirculation under the die lip, various constitutive models failed at a relatively low value of *Wi* because of the singularity in the velocity gradient at the contact line [28–30]. However, when recirculation was present, much higher *Wi* could be achieved before failure. In the latter case, the mode of failure was independent of the model details, i.e., the smallest eigenvalue of the conformation tensor reached zero in the region of strong extensional flow under the stretching section of the free surface. The maximum *Wi* achieved in all calculations increased as the molecules became stiffer. Pasquali and Scriven [19] also discussed that in *dilute polymer solutions* (in which case the conservation equations are coupled with the conformation tensor equation and the velocity field depends on the polymer stress), increase in the polymer viscosity or *Wi* result in the disappearance of recirculations under the die lip which ultimately lead to the failure of numerical computations.

Lee et al. [20] observed that in dilute polymer solutions, viscoelasticity increases the meniscus invasion and thus reduces the contact angle at the static contact line. They identified meniscus invasion as a possible mechanism for the onset of ribbing instabilities. A recent study by Romero et al. [23] has verified experimentally and theoretically that the viscoelastic nature of the fluid significantly reduces the contact angle due to meniscus invasion, leading to a non-uniform coating. Both Pasquali and Scriven [19] and Lee et al. [20] observed the formation of elastic stress boundary layers under the free surface and the failure of the numerical method at high *Wi*.

Bajaj et al. [25] have observed that the catastrophic failure of numerical simulations at high *Wi* does not occur if the coating flow is modelled with a micro-macro approach which uses kinetic theory based microscopic constitutive models. They also found that in ultra-dilute flow computations using a macroscopic constitutive equation, the maximum *Wi* corresponding to the catastrophic failure can be increased substantially by mesh refinement. However, the failure was found to be insensitive to the mesh refinement and the choice of constitutive model for dilute solutions. Bajaj et al. [25] have argued that the different behavior shown by dilute polymer solutions is due to the coupling between the velocity and the elastic stress that causes the

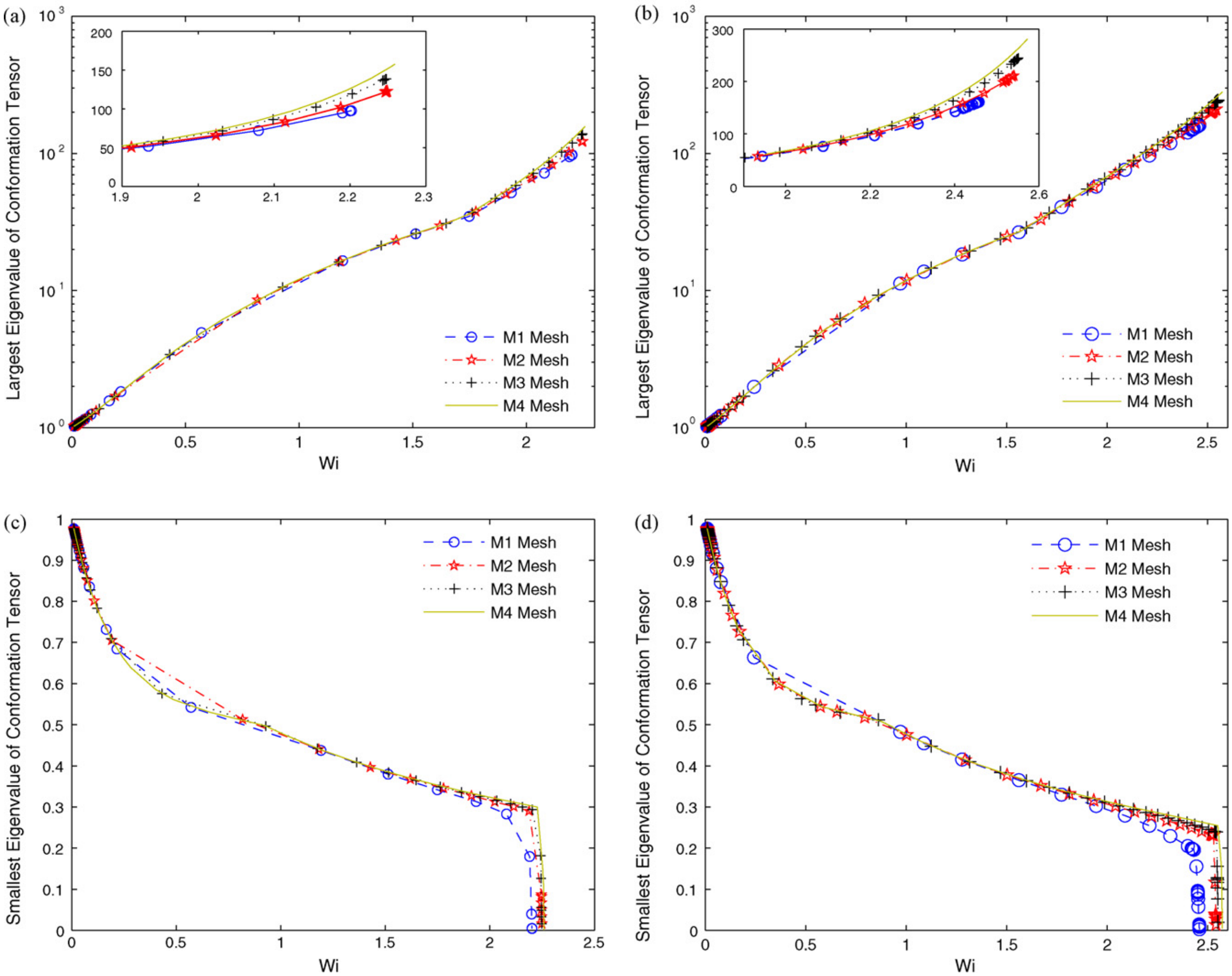

Fig. 3. Largest (a and b) and smallest (c and d) eigenvalues of the conformation tensor in the flow domain for an Oldroyd-B fluid. Inset shows the convergence of solutions at high *Wi*. $Ca = 0.1$, $Q = 0.3$. (a and c) $\beta = 0.25$ and (b and d) $\beta = 0.51$.

recirculation under the die lip to disappear at high *Wi*, exposing the inappropriate boundary condition applied on the momentum equation at the contact line.

While the coupling between flow and the flow induced microstructure in slot coating is yet to be examined, a recent study on roll coating of dilute polymer solutions has revealed that the presence of polymer can change dramatically the flow field (e.g. velocity field, recirculation, etc.) which ultimately leads to flow instabilities [24]. This kind of behavior is not expected for a ultra-dilute solution as the flow field is independent of the elastic stress. Zevallos et al. [24] have established that for a given flow condition and *Ca* in viscoelastic roll coating flows, there is always a critical *Wi* beyond which the normal stress difference at the stagnation point becomes positive, and the recirculation, which is present at low *Wi*, completely disappears. Due to the disappearance of recirculation, the flow close to the stagnation point becomes stronger and consequently, the normal stress difference at the free surface increases dramatically. This has been offered as an explanation of how liquid elasticity makes roll coating flow unstable at a high *Wi* [31,24].

The flow computations by Pasquali and Scriven [19], Lee et al. [20], Zevallow et al. [24] and Bajaj et al. [25] have furthered the understanding of the role of viscoelasticity on slot coating and general free surface flows. However, it is not yet clear why ultra-dilute polymer solutions differ from dilute ones in the mode of failure of numerical simulations at high *Wi* number. The primary aim of this paper is to understand how viscoelastic properties of the fluid affect the macroscopic and microscopic properties (e.g., the molecular stretch, the velocity field, recirculation under the die, the location of the stagnation point, etc.) leading to the observed unusual mesh convergence behavior. The stability criteria proposed by Graham [31] is applied to understand the role of viscoelasticity on the stability of slot coating.

To further examine the viscoelastic effect, results for flow computations of the low flow limit of slot coating is also presented. The low-flow limit is the minimum thickness that can be coated at a given substrate speed while maintaining a uniform coating [2,12,23,32,33]. Carvalho and Kheshgi [12] and Romero et al. [23] have discussed the design of a stable coating window for slot coating flows. Carvalho and Kheshgi [12]

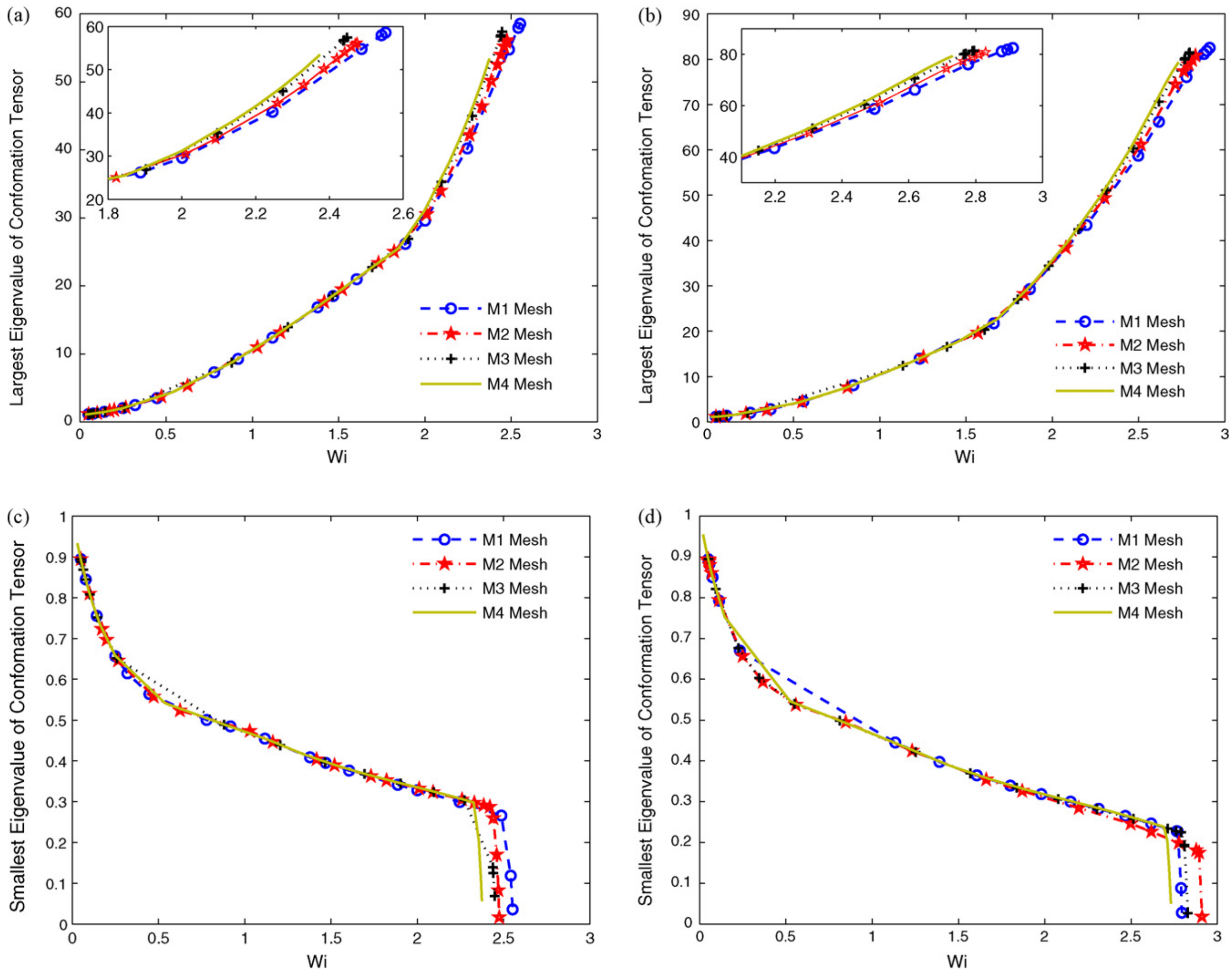

Fig. 4. Largest (a and b) and smallest (c and d) eigenvalues of the conformation tensor in the flow domain for the FENE-P fluid. Inset shows the convergence of solutions at high *Wi*. $Ca = 0.1$, $Q = 0.3$, $b = 50$. (a and c) $\beta = 0.25$ and (b and d) $\beta = 0.51$.

have extended the work on the low-flow limit of Ruschak [2] and Landau and Levich [34] by conducting experiments and by carrying out numerical simulations at much higher values of *Re* and *Ca* for a Newtonian liquid. Both experiment and numerical results predict that the viscocapillary model proposed by Landau and Levich [34] is useful only for low *Ca* and *Re*. Carvalho and Kheshgi [12] found that at higher *Ca*, the viscocapillary model underpredicts the low flow limit for inertialess flows. Romero et al. [23] extended the work of Carvalho and Kheshgi [12] to viscoelastic liquids and predicted that the critical conditions for the onset of the low-flow limit are strong functions of viscoelasticity of the fluid and the ratio of solvent to the solution viscosity (β). Using a strain-type constitutive equation [35] to capture the behavior of their experimental viscoelastic liquid, they demonstrate that viscoelasticity reduces the size of the coating window. Subsequently, Romero et al. [33] have shown that for the Oldroyd-B and FENE-CR fluids, at $Wi \sim 0.1$, viscoelasticity widens the coating window, while a further increase in *Wi* yields higher viscoelastic stresses leading to a narrower operability window.

In this work, Oldroyd-B and FENE-P constitutive models are used to investigate the effect of viscoelasticity on the low-flow limit in terms of the Elastocapillary number, $Ec \equiv Wi/Ca$. The use of *Ec* is particularly important for a proper representation of experimental data on the low flow limit for a given fluid and it is analogous to the property number ($P_\mathrm{p} = Re/Ca$) defined by Carvalho and Kheshgi [12] to investigate the effect of inertial forces. Here, we examine the low-flow limit for various values of *Ec* and β.

The next section presents an overview of the basic macroscopic conservation and constitutive equations. The finite element method to solve the set of governing equations is described in Section 3. Section 4 analyzes the flow under the downstream section of a slot coater, while Section 5 summarizes the central conclusions of this paper.

2. Governing equations

2.1. Transport equations

The transport equations governing mass and momentum in steady, isothermal and incompressible flows of dilute polymer solutions in the absence of any external forces are:

$$0 = \nabla \cdot \mathbf{v} \tag{1}$$

$$0 = \rho \mathbf{v} \cdot \nabla \mathbf{v} - \nabla \cdot \mathbf{T} - \nabla \boldsymbol{\Theta} \tag{2}$$

where $\mathbf{v}$ is the liquid velocity, ρ the liquid density, and $\boldsymbol{\Theta}$ is the potential of body force per unit volume. The total stress tensor: $\mathbf{T} = -p\mathbf{I} + \boldsymbol{\tau} + \boldsymbol{\sigma}$, where p is the pressure, $\mathbf{I}$ the identity tensor, $\boldsymbol{\tau}$ the viscous stress tensor and $\boldsymbol{\sigma}$ is the polymer contribution to the total stress tensor. The viscous stress: $\boldsymbol{\tau} = 2\eta_\mathrm{S}\mathbf{D}$, where $\mathbf{D} = (1/2)(\nabla\mathbf{v} + \nabla\mathbf{v}^\mathrm{T})$ is the rate of strain tensor and η_S is Newtonian viscosity.

The polymer contribution to the total stress is evaluated by using the general conformation tensor based constitutive equations [19]. The conformation tensor $\mathbf{M}$ is a microstructural variable that represents the local expectation value of the stretch and orientation of polymer molecules [19,36–38].

The steady state transport equations for the evolution of dimensionless conformation tensor are [39]:

$$\begin{aligned} 0 = {} & \mathbf{v} \cdot \nabla \mathbf{M} - 2\xi \frac{\mathbf{D} : \mathbf{M}}{\mathbf{I} : \mathbf{M}} \mathbf{M} - \zeta \left(\mathbf{M} \cdot \mathbf{D} + \mathbf{D} \cdot \mathbf{M} - 2 \frac{\mathbf{D} : \mathbf{M}}{\mathbf{I} : \mathbf{M}} \mathbf{M} \right) \\ & - \mathbf{M} \cdot \mathbf{W} - \mathbf{W}^\mathrm{T} \cdot \mathbf{M} + \frac{1}{\lambda} (g_0 \mathbf{I} + g_1 \mathbf{M} + g_2 \mathbf{M}^2) \end{aligned} \tag{3}$$

where $\mathbf{W} = 1/2(\nabla\mathbf{v} - \nabla\mathbf{v}^\mathrm{T})$ is the vorticity tensor, and λ is the characteristic relaxation time of the polymer. The constitutive function $\xi(\mathbf{M})$ represents the polymer's resistance to stretching along its backbone, $\zeta(\mathbf{M})$ represents the polymer's resistance to rotation with respect to its neighbors and $g_0(\mathbf{M})$, $g_1(\mathbf{M})$, and $g_2(\mathbf{M})$ define the rate of relaxation of polymer segments.

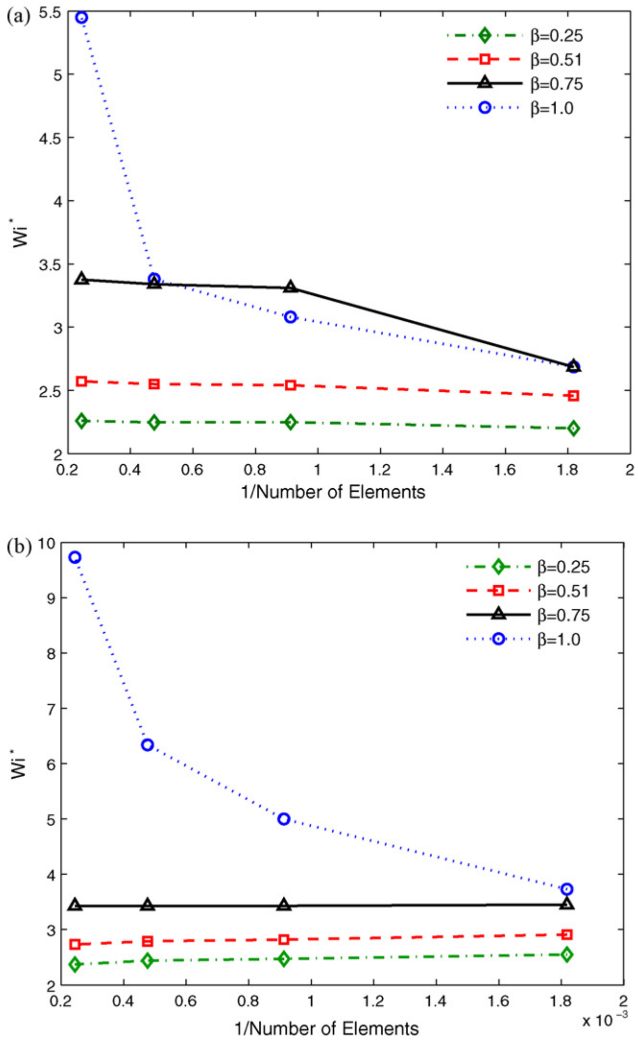

Fig. 5. Change in Wi^* with number of elements for the Oldroyd-B (a) and FENE-P (b) models. $Ca = 0.1$, $Q = 0.3$, $b = 50$.

Table 1
Constitutive functions for Oldroyd-B and FENE-P models

	ξ	χ	g_0	g_1	g_2	a
Oldroyd-B	1	1	-1	1	0	$\frac{G}{2}\mathrm{tr}\mathbf{M}$
FENE-P	1	1	-1	$\frac{b-1}{b-\mathrm{tr}\mathbf{M}/3}$	0	$\frac{3G(b-1)}{2}\ln\left(\frac{b-1}{b-\mathrm{tr}\mathbf{M}/3}\right)$

The elastic stress, $\boldsymbol{\sigma}$, is related to the conformation tensor by [39]:

$$\boldsymbol{\sigma} = 2(\xi-\zeta)\frac{\mathbf{M}}{\mathbf{I}:\mathbf{M}}\mathbf{M} : \frac{\partial a}{\partial \mathbf{M}} + 2\zeta\mathbf{M}\cdot\frac{\partial a}{\partial \mathbf{M}} \tag{4}$$

where $a(\mathbf{M})$ is the Helmholtz free energy per unit volume of the liquid. Table 1 contains the constitutive functions $\xi(\mathbf{M})$, $\zeta(\mathbf{M})$, $g_0(\mathbf{M})$, $g_1(\mathbf{M})$, $g_2(\mathbf{M})$, and $a(T,\mathbf{M})$ for the Oldroyd-B and FENE-P models (see Ref. [39] for more details).

2.2. Mesh generation

A boundary fitted elliptic mesh generation method is used to construct the mapping between the physical domain and a reference or computational domain [5,40]. The mapping obeys

$$\nabla\cdot\tilde{\mathbf{D}}\cdot\nabla\boldsymbol{\xi} = 0 \tag{5}$$

where $\boldsymbol{\xi}$ is the position in the computational domain and the dyadic $\tilde{\mathbf{D}}$ is a symmetric positive definite tensor which controls the spacing of the coordinate lines [19].

2.3. Problem description and boundary conditions

Fig. 1 shows the downstream section of a slot coater. The upper wall is the die wall and the lower solid wall is the moving web. The liquid is being coated on the moving web. In pre-metered slot coating, the flow rate at the inlet and the final

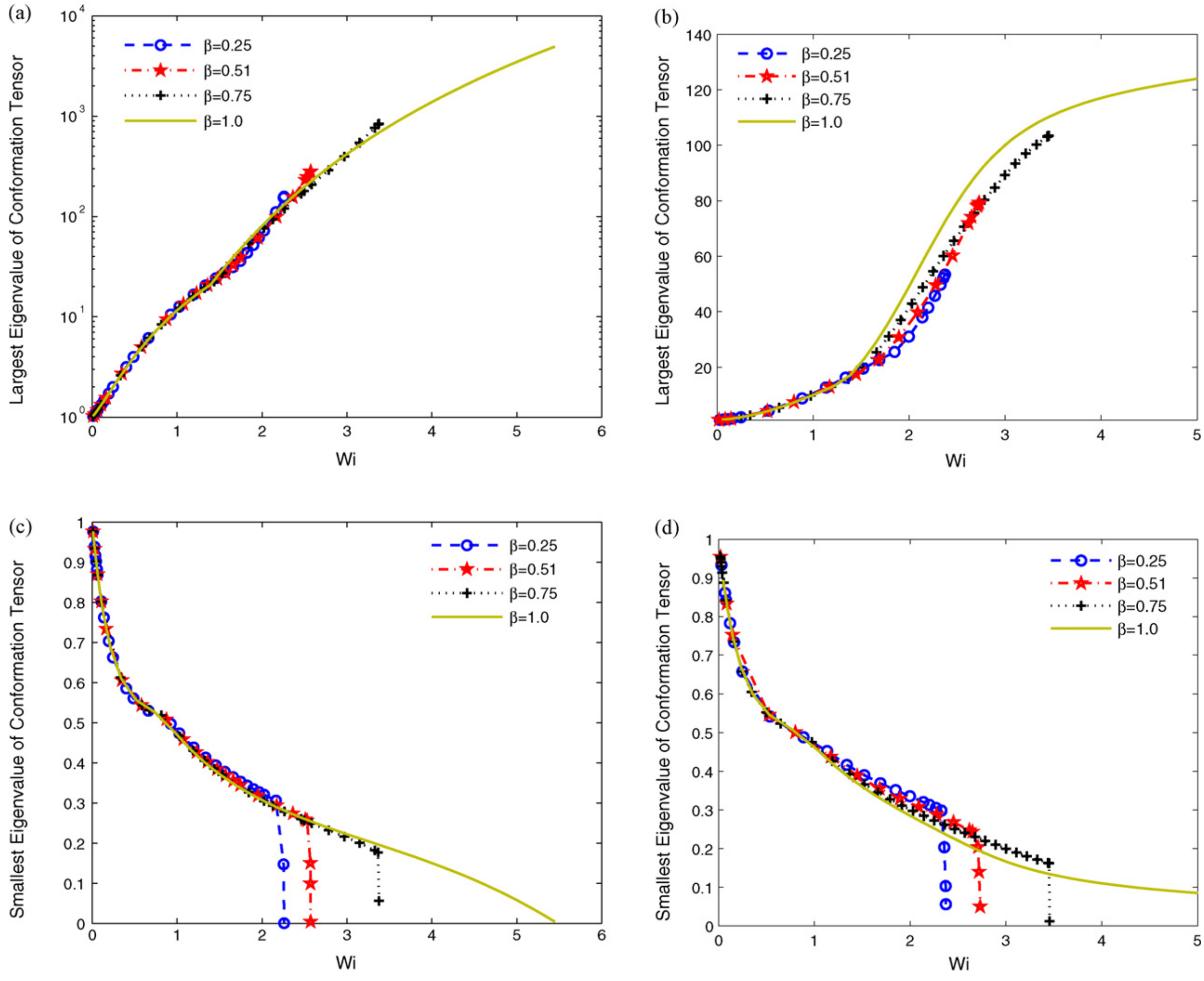

Fig. 6. Effect of viscosity ratio (β) on the polymer conformation for the Oldryod-B (a and c) and FENE-P (b and d) models. For $\beta = 1$, the stretch is plotted up to $Wi = 5$ for the FENE-P model. Note that the maximum Wi for $\beta = 1$ is ~ 9 (see Fig. 3 of Ref. [25]). Computations are carried out using the M4 mesh. $Ca = 0.1$, $Q = 0.3$, $b = 50$. (a and b) Largest eigenvalue and (c and d) smallest eigenvalue.

coating thickness are known. These transport equations and mesh equations governing the slot coating flow are solved with the following boundary conditions.

2.3.1. Boundary Conditions on Transport Equations:

(1) A no slip boundary condition is applied at the solid walls ($\mathbf{v} = 0$ at the die wall and, $v_x =$ web velocity; $v_y = 0$ at the web).

(2) The force balance at the free surface is imposed on the momentum equation through the following traction boundary condition:

$$\mathbf{n} \cdot \mathbf{T} = -p_{\mathrm{a}}\,\mathbf{n} + \varsigma\,\mathbf{n}\,(\nabla_{\mathrm{II}} \cdot \mathbf{n}) \qquad (6)$$

where ∇_{II} denotes the surface divergence operator [41] $\nabla_{\mathrm{II}} = (\mathbf{I} - \mathbf{n}n) \cdot \nabla$, p_{a} the ambient pressure in the gas phase, ς the surface tension and $\mathbf{n}$ is the unit vector normal to the free

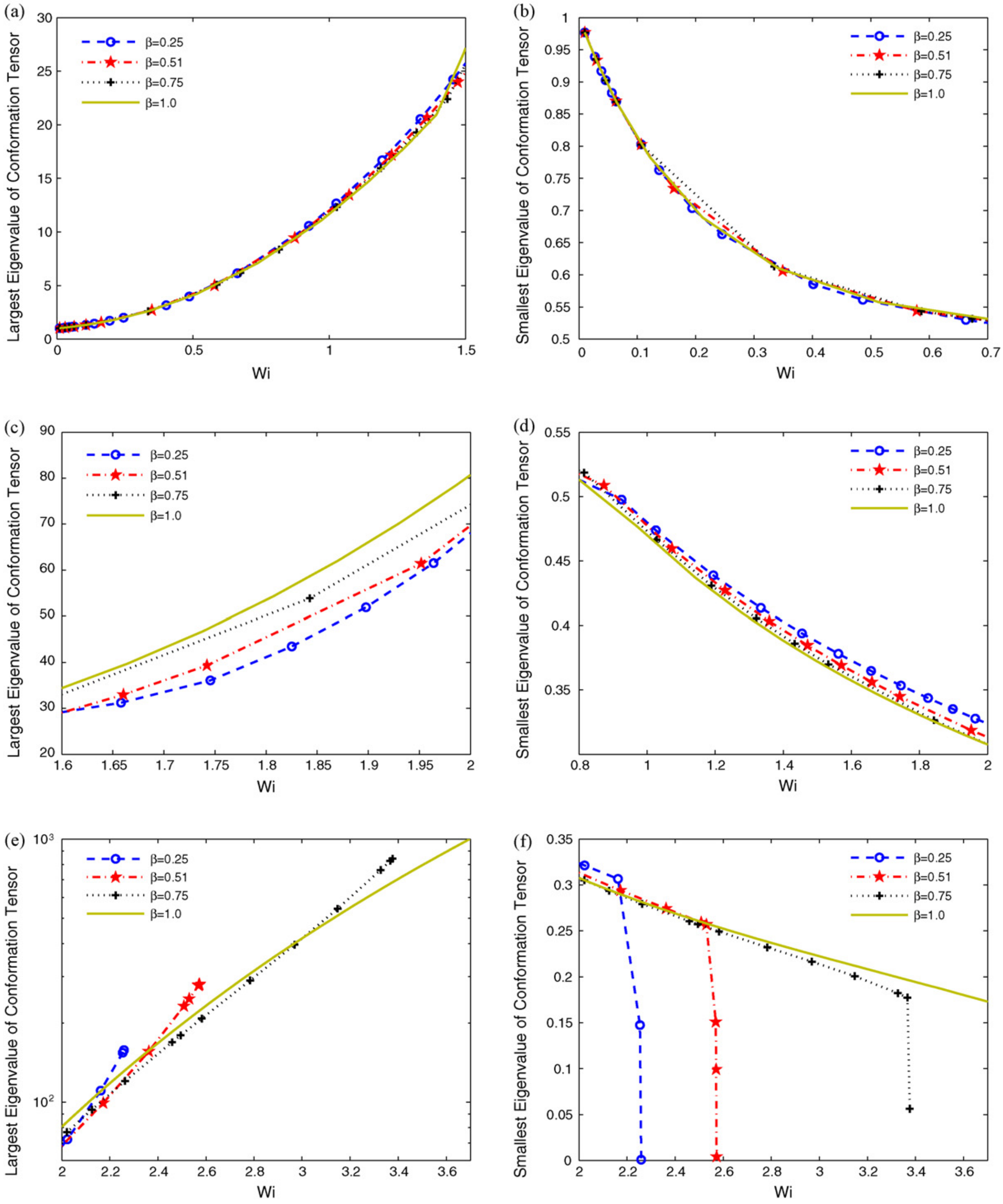

Fig. 7. Effect of viscosity ratio (β) on the conformation of the molecule for an Oldroyd-B fluid. Zoomed images of Fig. 6. $Ca = 0.1$, $Q = 0.3$. (a) Largest eigenvalue, $Wi \lesssim 1.5$, (b) smallest eigenvalue, $Wi \lesssim 0.7$, (c) largest eigenvalue, $1.5 \lesssim Wi \lesssim 2.0$, (d) smallest eigenvalue, $0.7 \lesssim Wi \lesssim 2.0$, (e) largest eigenvalue, $Wi \gtrsim 2$ and (f) smallest eigenvalue, $Wi \gtrsim 2.0$.

surface. The tangential component of Eq. (6) is the vanishing shear stress, $\mathbf{tn} : \mathbf{T} = 0$, at the free surface.

(3) The flow rate at the inflow boundary is imposed by specifying a velocity profile $\mathbf{v} = f(\mathbf{x})$.
(4) The fully developed flow condition at the outflow boundary is imposed naturally as $\mathbf{n} \cdot \nabla \mathbf{v} = 0$.
(5) The conformation transport equation (Eq. (3)) is a hyperbolic equation. In fully developed flow, the polymer conformation does not change along streamlines [19,42] and thus,

$$\mathbf{v} \cdot \nabla \mathbf{M} = 0 \tag{7}$$

holds at the inflow boundary.

2.3.2. Boundary conditions on mesh equations

The following boundary conditions are used to solve the mesh equation (Eq. (5)):

(1) The location of nodes on the boundary is fixed at the inflow and on the two solid walls.
(2) At the free surface, the following kinematic boundary condition is applied.

$$\mathbf{n} \cdot \mathbf{v} = 0 \tag{8}$$

More details on mesh boundary conditions can be found in Ref. [19].

3. Dimensionless numbers

Dimensional analysis of the system of equations suggests that it is convenient to introduce five dimensionless numbers, which are combinations of the various macroscopic model parameters ρ, H_0, q, η_S, ς, $\eta_{p,0}$, v, λ, etc. Here, H_0 is the die gap, q the flow rate, η_S the solvent viscosity, $\eta_{p,0}$ the polymer contribution to the zero shear viscosity, and v is the web velocity. These dimensionless numbers are:

(1) The Reynolds number, $Re = \rho v H_0/(\eta_S + \eta_{p,0})$.
(2) The Capillary number, $Ca = (\eta_S + \eta_{p,0})v/\varsigma$.
(3) The viscosity ratio, $\beta = \eta_S/(\eta_S + \eta_{p,0})$.
(4) The Weissenberg number, $Wi = \lambda v/H_0$.
(5) The dimensionless feed flow rate, $Q = q/(vH_0)$
(6) The Elastocapillary number, $Ec = Wi/Ca = \lambda\varsigma/(\eta_S + \eta_{p,0})H_0$. This dimensionless number is useful because it depends only on fluid properties and slot width and is independent of the web velocity (unlike Ca and Wi). To investigate the effect of viscoelasticity on the low flow limit of inertialess slot coating flow, the parameter space to be explored is either a combination of Ec, Ca and β or a combination of Ec, Wi and β. Both combinations ensure that all the relevant forces are taken into account and, conveniently, the web velocity is related solely to a single dimensionless parameter (either Ca or Wi).

All simulations are performed at $Re = 0$. The FENE-P simulation are carried at $b = 50$, ensuring that the behavior of FENE-P model differs from the Oldroyd-B fluid. The dimensionless numbers that are varied in this work are Ca, β, Wi and Ec. Simulations to predict critical conditions for the low-flow limit are performed at different values of Ca, Ec and die gap to coating thickness ratio (H_0/t), where t is the coating thickness (Fig. 1).

4. Computational method

The mesh equation and transport equations are discretized by using the DEVSS-TG/SUPG mixed finite element method [19] which is a stable formulation based on the earlier work by Guénette and Fortin [43] and Szady [44]. The DEVSS-TG formulation involves the introduction of an additional variable, the velocity gradient $\mathbf{L}$. Continuous biquadratic basis functions represent velocity and position, linear discontinuous basis functions represent pressure and continuous bilinear basis functions are used for the interpolated velocity gradient and conformation tensor. The DEVSS-TG/SUPG spatial discretization results in a large set of coupled non-linear algebraic equations, which is solved by Newton's method with analytical Jacobian, frontal solver, and first order arclength continuation in parameters [19].

5. Results

5.1. Dilute v/s ultra-dilute solutions

This study employs four different meshes used previously to study slot coating flow by micro-macro methods [25]. Details

Table 2
Meshes used for slot coating flow computations

Mesh	Number of elements	Number of nodes	Degrees of freedom ($\mathbf{x}$, $\mathbf{v}$, p, $\mathbf{M}$, $\mathbf{L}$)
M1	550	2,311	15,712
M2	1096	4,539	30,836
M3	2100	8,611	58,392
M4	4105	16,717	113,215

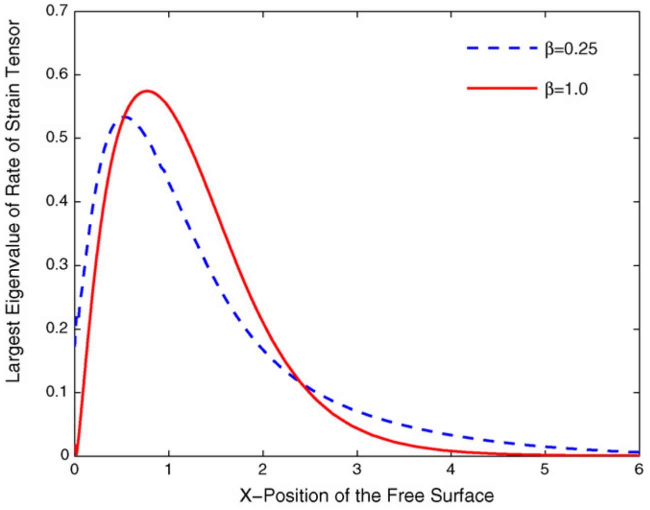

Fig. 8. Effect of viscosity ratio on the largest eigenvalue of the rate of strain tensor along the free surface for an Oldroyd-B fluid. $Wi = 2.0$, $Ca = 0.1$, $Q = 0.3$.

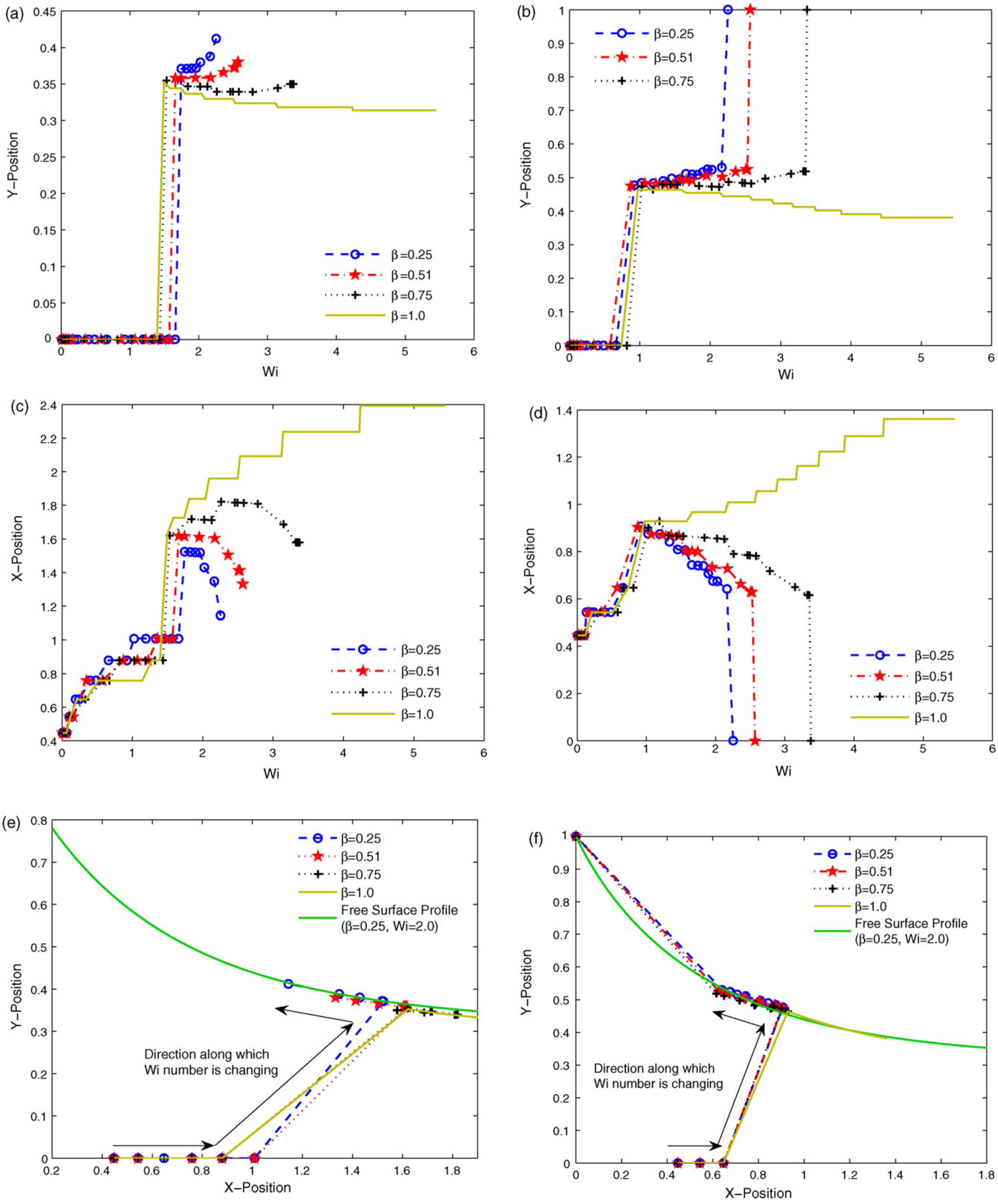

Fig. 9. Change in spatial position of the largest (a, c and e) and smallest (b, d and f) eigenvalues of the conformation tensor as a function of *Wi* for an Oldroyd-B fluid. $Ca = 0.1$, $Q = 0.3$.

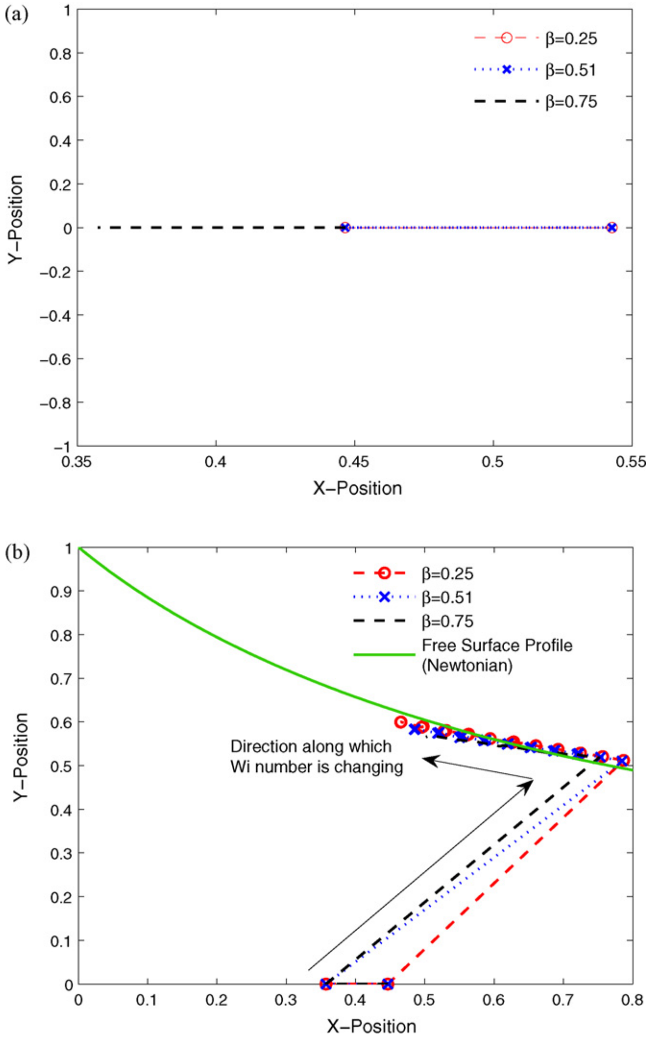

Fig. 10. Change in the spatial position of the maximum molecular shear (a) and extension rate (b) with *Wi* number for different values of β. The Newtonian free surface profile is shown for reference. $Ca = 0.1$, $Q = 0.3$.

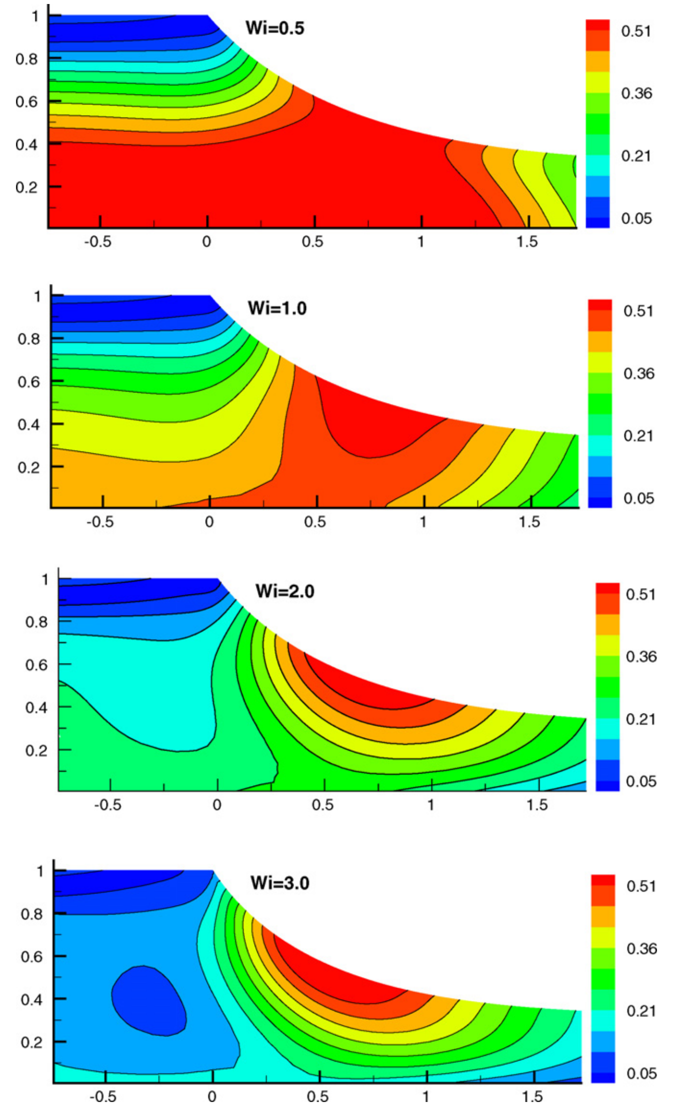

Fig. 11. Molecular extension rate as a function of *Wi* for an Oldroyd-B fluid. $Ca = 0.1$, $Q = 0.3$, $\beta = 0.75$.

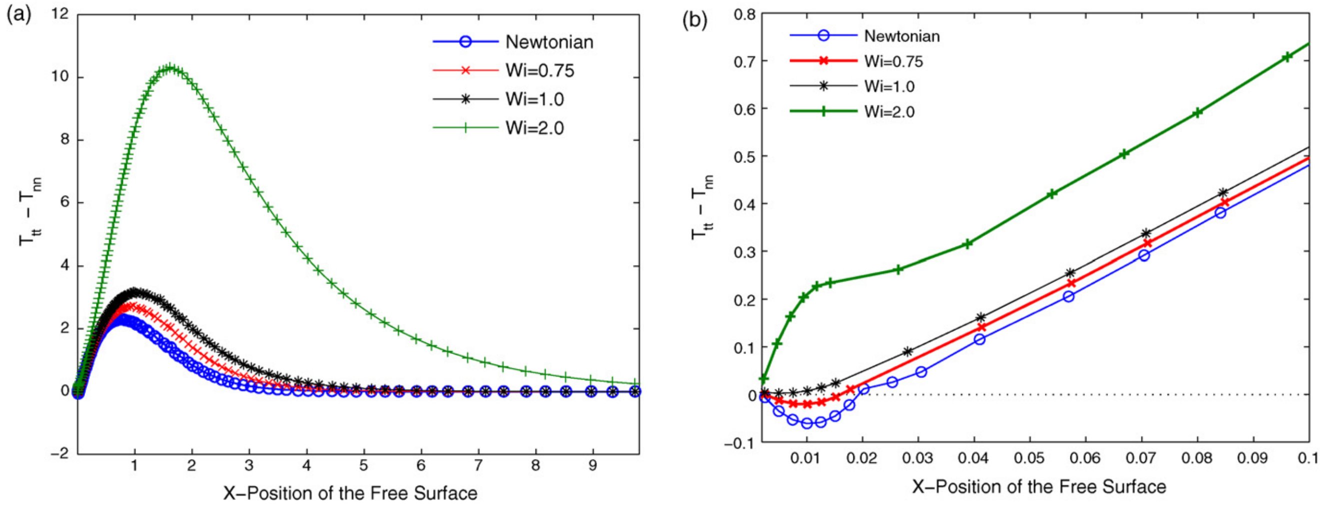

Fig. 12. Normal stress difference along the free surface as a function of *Wi* for an Oldroyd-B fluid. (b)The close-up image of (a) near to the static contact line. $Ca = 0.1$, $Q = 0.3$, $\beta = 0.75$.

on meshes M1, M2, M3, and M4 are given in Table 2. Chiefly, the four meshes differ in the density of elements near the static contact line and near the air/liquid interface.

Bajaj et al. [25] have presented the mesh convergence results in terms of the eigenvalues of the conformation tensor. The eigenvalues of the conformation tensor are always real and positive because the conformation tensor is symmetric and positive definite [19]. They found that computations for dilute ($\beta = 0.75$) and ultra-dilute ($\beta = 1.0$) solutions failed at a critical Weissenberg number (Wi^*) when one of the eigenvalues became negative somewhere in the flow domain. In dilute solutions, Wi^* was independent of mesh refinement and choice of constitutive model. Conversely, Wi^* depended strongly both on mesh refinement and the choice of constitutive model in ultra-dilute solutions (see Figs. 3, 5, 10 and 11 of Ref. [25]). Contrary to the common belief, this suggests that in dilute polymer solutions, mesh refinement does not resolve stress boundary layers formed under the stretching section of the free surface at high Wi (see Fig. 2). Here, we extend the work of [25] to analyze a wider range of viscosity ratios to gain a clear insight into the behavior of dilute and ultra-dilute solutions.

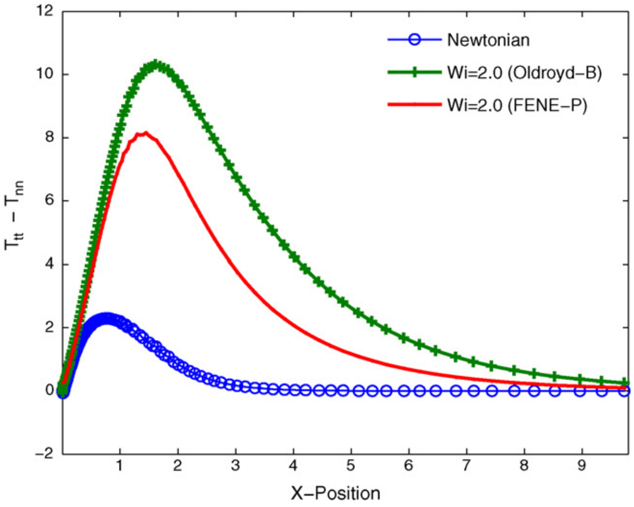

Fig. 13. Normal stress difference along the free surface for different constitutive equations. $Ca = 0.1$, $Q = 0.3$, $\beta = 0.75$, $b = 50$.

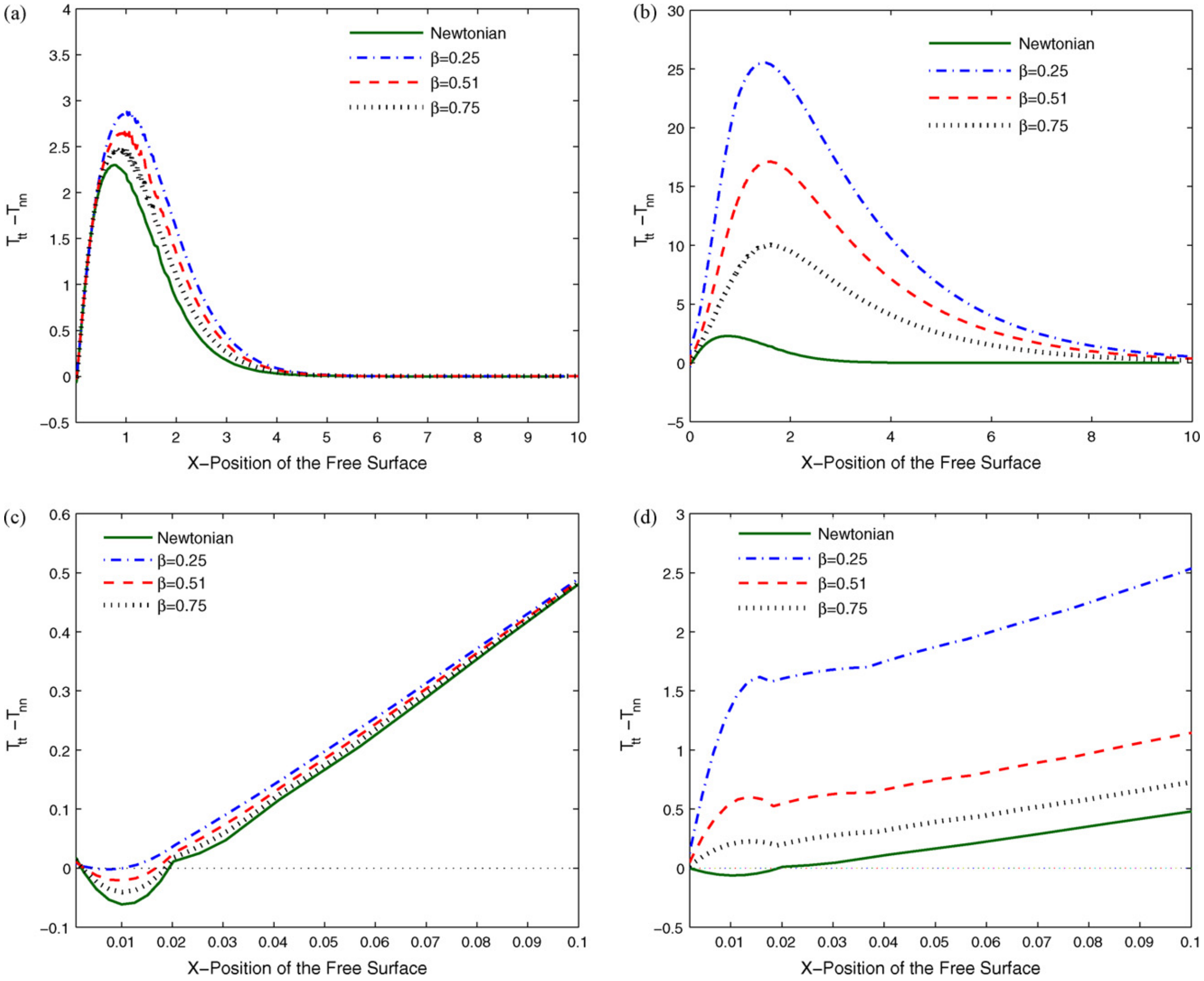

Fig. 14. Normal stress difference along the free surface (a and b) and near the contact line (c and d) as a function of viscosity ratio for an Oldroyd-B fluid. $Ca = 0.1$, $Q = 0.3$. (a and c) $Wi = 0.5$ and (b and d) $Wi = 2.0$.

Figs. 3 and 4 show the mesh convergence of computational results for the Oldroyd-B and FENE-P models at two different values of β. As for $\beta = 0.75$, lower β values also show that Wi^* is independent of mesh and constitutive model. However, mesh converged results are obtained at least up to $Wi = 2$ at all four values of β. The mesh independence of Wi^* is more clearly shown in Fig. 5 for both the Oldroyd-B and FENE-P models. Wi^* decrease at lower viscosity ratio (Fig. 5).

The unusual mesh convergence behavior of dilute and ultra-dilute solutions with regards to its sensitivity to mesh refinement and choice of constitutive equations poses interesting questions. To probe these differences, a detailed analysis of the effect of viscosity ratio on flow properties is presented in the next section.

5.1.1. *Effect of viscosity ratio on the polymer conformation*

Fig. 6 shows the effect of the viscosity ratio β on the stretch of polymer molecules as a function of Wi for the Oldroyd-B and FENE-P models. These figures display the largest and smallest eigenvalues of conformation tensor in the flow domain (irrespective of location). For clarity, the same data are broken up in Fig. 7 into different regimes of magnitude of Wi for the Oldroyd-B model. Fig. 7(a) shows that when Wi is below ~ 1.5, the largest eigenvalue of the conformation tensor is independent of viscosity ratio. Beyond $Wi \sim 1.5$, (Fig. 7(c)), the rate of stretching decreases with decreasing β (which corresponds to an increasing concentration of polymer). At $Wi > 2$ (Fig. 7(e)), the stretch in dilute system is lower than that in the ultra-dilute, as long as the computations hold accurately (Fig. 7(f)).

Fig. 8 shows the effect of viscosity ratio on the largest eigenvalue of the rate of strain tensor. By decreasing the viscosity ratio, the largest eigenvalue of the rate of strain tensor decreases which explains the decrease in the rate of stretching with decreasing viscosity ratio (Fig. 7(c)).

The smallest eigenvalue of the conformation tensor shows a weaker dependence on the viscosity ratio in the range of Wi from 0 to 2 (Fig. 7(b) and (d)) compared to the rate of change of the largest eigenvalue. However, for the Wi at which the rate of change of the largest eigenvalue diverges, the minimum eigenvalue becomes zero and the conformation tensor eventually loses its positive definiteness (Fig. 7(f)).

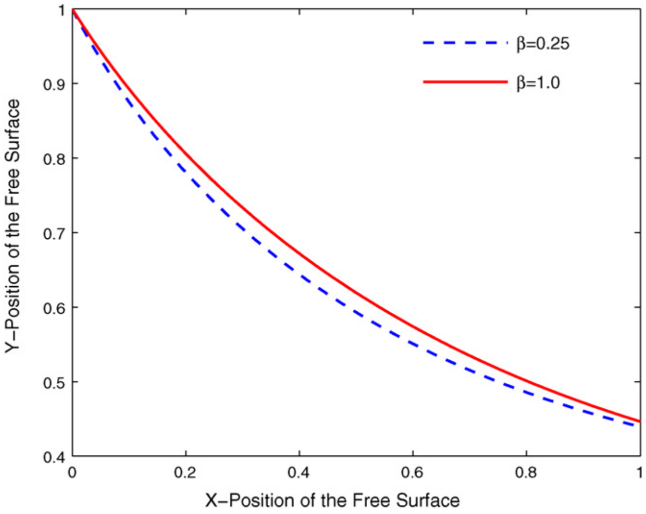

Fig. 15. Effect of polymer viscosity on the shape of the free surface for an Oldroyd-B fluid. $Wi = 2.0$, $Ca = 0.1$, $Q = 0.3$.

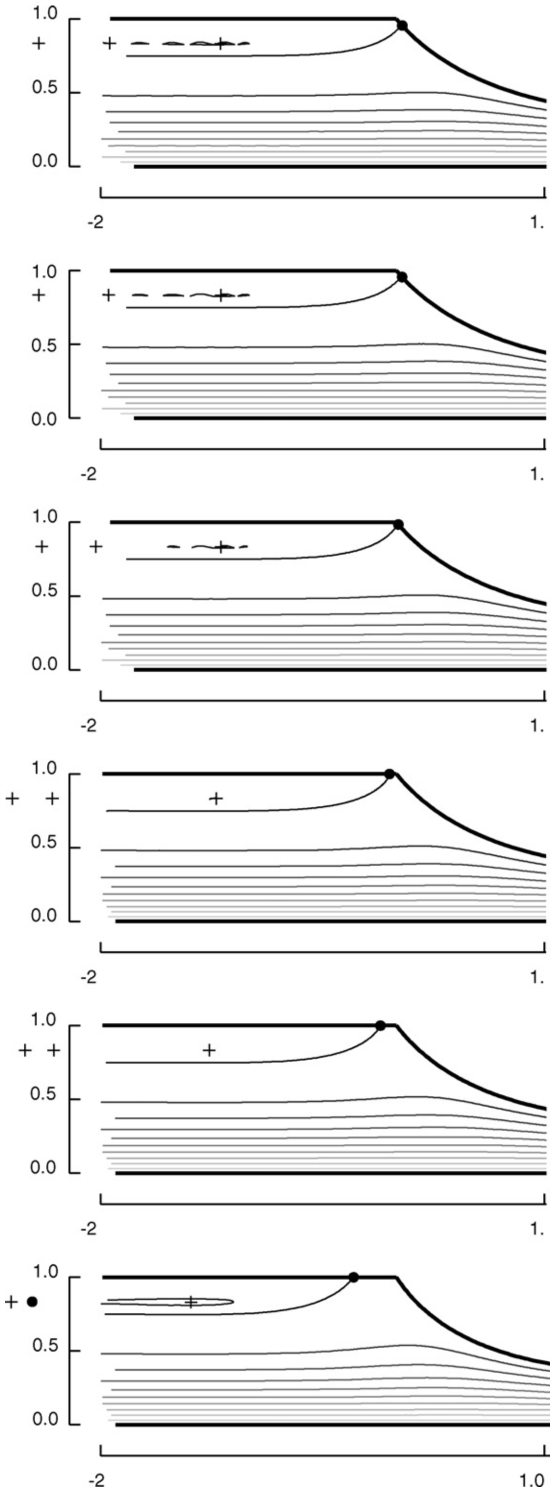

Fig. 16. Movement of the stagnation point for an Oldroyd-B liquid. The dark filled circle denotes the stagnation point. $Ca = 0.1$, $Q = 0.3$, $\beta = 0.75$. From top to bottom $Wi = 0.0$ (Newtonian), 0.75, 1.0, 1.5, 2.0 and 3.0.

Another interesting feature of Fig. 6 is that both the largest and smallest eigenvalues show a point of inflection at $Wi_{\mathrm{L}}^* \sim 1.5$

and $Wi_\mathrm{S}^* \sim 0.7$, respectively; these values are independent of the choice of constitutive equation as shown in Fig. 6(b) and (d) for the FENE-P model. The two different regimes of the rate of stretching near Wi_L^* and Wi_S^*, can be explained by examining the location of the largest and smallest eigenvalues of the conformation tensor in the flow domain (Fig. 9). When $Wi < Wi_\mathrm{L}^*$, the Y-coordinate of the location of the largest eigenvalue in the flow domain remains at $Y = 0$ (on the moving web) (Fig. 9(a)) independent of the viscosity ratio. On the web, the stretch of the molecules is dominated by shearing flow kinematics. Beyond Wi_L^*, the largest eigenvalue abruptly jumps from the web to the free surface as shown in Fig. 9(e). For clarity, the free surface profile is plotted at $\beta = 0.25$, $Wi = 2.0$ in Fig. 9(e). On the free surface, the flow kinematics is extensional in nature. Different flow kinematics at the web and the free surface lead to the different rates of change of the largest eigenvalue around Wi_L^*.

The transition in position of the smallest eigenvalue from the web to the free surface occurs at $Wi \sim Wi_\mathrm{S}^*$ as shown in Fig. 9(f). However, for dilute solutions ($\beta < 1$), the position of the smallest eigenvalue once more abruptly changes from the free surface to the static contact line when the smallest eigenvalue approaches zero (see Fig. 9(b)). The change in position from the free surface to the static contact line occurs at a higher Wi at higher viscosity ratio. When $\beta = 1$, the smallest eigenvalue always remains on the free surface for $Wi > Wi_\mathrm{S}^*$. The conformation tensor always loses it positive definiteness at the static contact line for $\beta < 1$, which is different from simulation of ultra-dilute solutions ($\beta = 1$) where the conformation tensor loses its positive definiteness under the stretching section of the free surface (as reported earlier by Pasquali and Scriven [19]). The behavior of the location of the eigenvalues for the FENE-P model with $b = 50$ virtually coincides with those obtained with the Oldroyd-B model.

The X-coordinate of the largest (Fig. 9(c)) and smallest (Fig. 9(d)) eigenvalues indicate that both eigenvalues move on the free surface towards the die wall as Wi increase when $\beta < 1$. This behavior can be understood by considering the position of the maximum molecular extension rate (shown in Fig. 10). The mean ensemble molecular extension and shear rates are

$$\dot{\epsilon} \equiv |\mathbf{m}_3\mathbf{m}_3 : \mathbf{D}|; \qquad \dot{\gamma} \equiv |\mathbf{m}_1\mathbf{m}_3 : \mathbf{D}| \tag{9}$$

where $\mathbf{m}_1$ and $\mathbf{m}_3$ are the eigenvectors associated with the smallest and largest eigenvalues of the conformation tensor, respectively [19]. Fig. 10(a) shows that for an Oldroyd-B fluid, the maximum molecular shear rate always remains on the web at all Wi (see Refs. [19,23]); Fig. 10(b) shows the evolution of the location of the maximum molecular extension rate as a function of Wi. At low Wi, the molecules stretch predominantly near the web, where the rate of strain is highest and the flow is dominated by shear. At high Wi, the polymer molecules becomes more and more stretched and a thin layer of high molecular extension grows at the free surface. The maximum molecular extension rate always occur under the stretching section of the free surface, i.e., downstream of the stagnation point (Fig. 11).

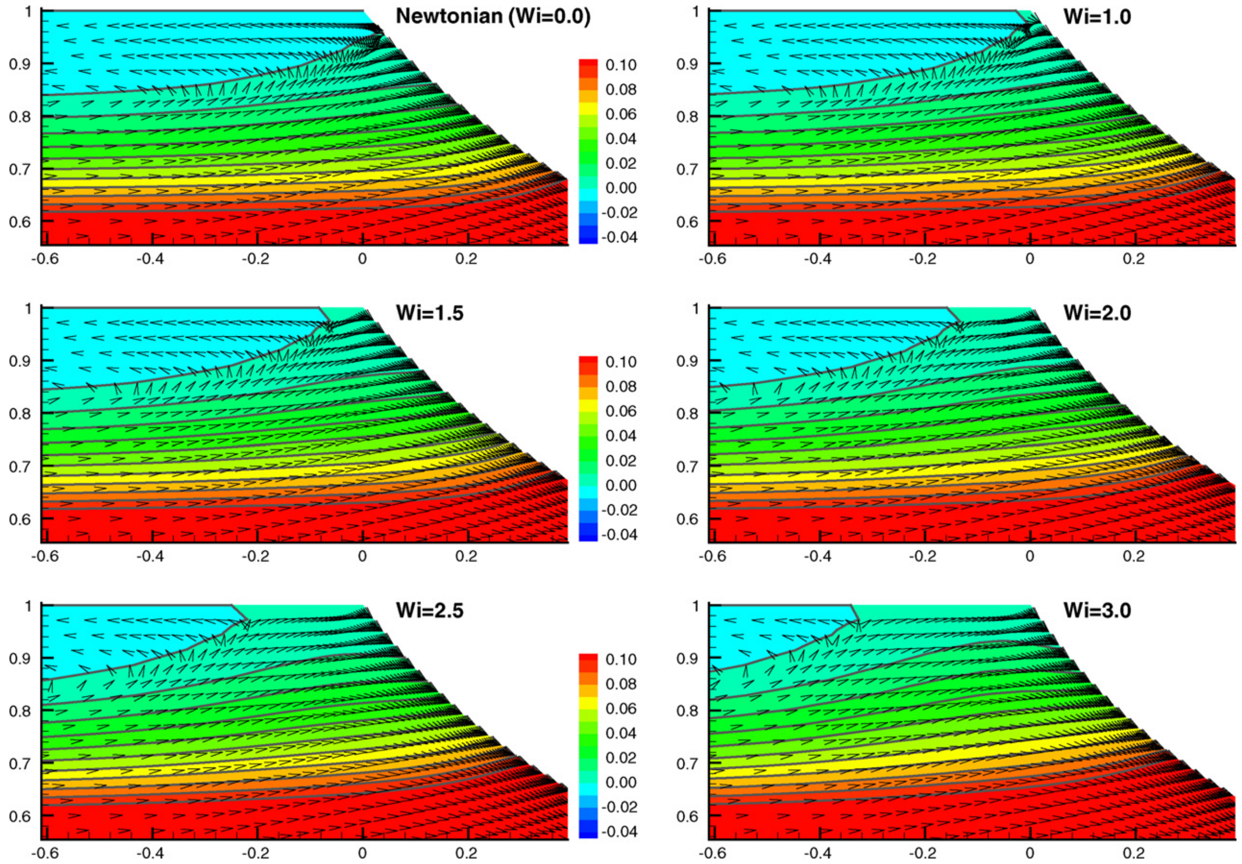

Fig. 17. Change in velocity profile by changing the Wi for an Oldroyd-B fluid. $Ca = 0.1$, $Q = 0.3$, $\beta = 0.75$.

An abrupt change in the location of the highest molecular extension rate explains why the largest and smallest eigenvalues of conformation tensor suddenly move from the web to the free surface.

Fig. 10(b) also shows that the maximum molecular extension rate moves upstream towards the static contact line, which explains behavior of the the X-position of the largest and smallest eigenvalues of the conformation tensor in Fig. 9.

5.1.2. *Effect of viscosity ratio on the macroscopic flow*

The viscoelastic nature of the fluid strongly affects the flow field in the vicinity of the static contact line. The change in the flow behavior is analyzed here in terms of the stability criterion proposed by Zevallos et al. [24] to examine the stability of roll coating. Zevallos et al. [24] combined the stability criteria proposed by Pitts and Greiller [14] for Newtonian film splitting flow with the stability mechanism proposed by Graham [31] for viscoelastic free surface flows and showed that for given flow conditions, an increase in Wi leads to the disappearance of the recirculation under the free surface at the film split location. This yields a positive normal stress difference at the film split and promotes instability.

The difference between the streamwise (T_{tt}) and crossstream (T_{nn}) normal stress components along the free surface is plotted against Wi in Fig. 12. $\mathbf{T}$ is the sum of pressure, viscous and elastic stresses. As Wi increases, the normal stress difference ($T_{tt} - T_{nn}$) along the free surface grows. Fig. 12(b) shows that near the static contact line, the normal stress difference is negative ($T_{nn} > T_{tt}$) at small Wi and changes sign beyond $Wi \sim 1$. This happens because as Wi grows, the stagnation point moves from the free surface to the die wall. Fig. 13 shows that the normal stress difference for the FENE-P model is smaller than the Oldryod-B model for $b = 50$.

Fig. 14 displays the effect of the viscosity ratio on normal stress difference at two different $Wi (Wi = 0.5, 2.0)$, for an Oldroyd-B liquid. At a given Wi, the normal stress difference increases with decreasing β. Fig. 14(c) and (d) shows that for a given Wi, a reduction in β leads to a positive normal stress difference in the vicinity of the static contact line. Similar behavior was observed for the FENE-P model.

Fig. 15 shows the effect of viscosity ratio on the shape of the free surface. For the parameters studied in this work, the shape of free surface is not significantly altered by viscoelasticity. However, close to the static contact line the free surface moves into the die as viscoelasticity increases, as predicted earlier by Lee et al. [20] and Romero et al. [23]. This movement causes a reduction in the contact angle and ultimately would yield the detachment of the free surface from the die wall.

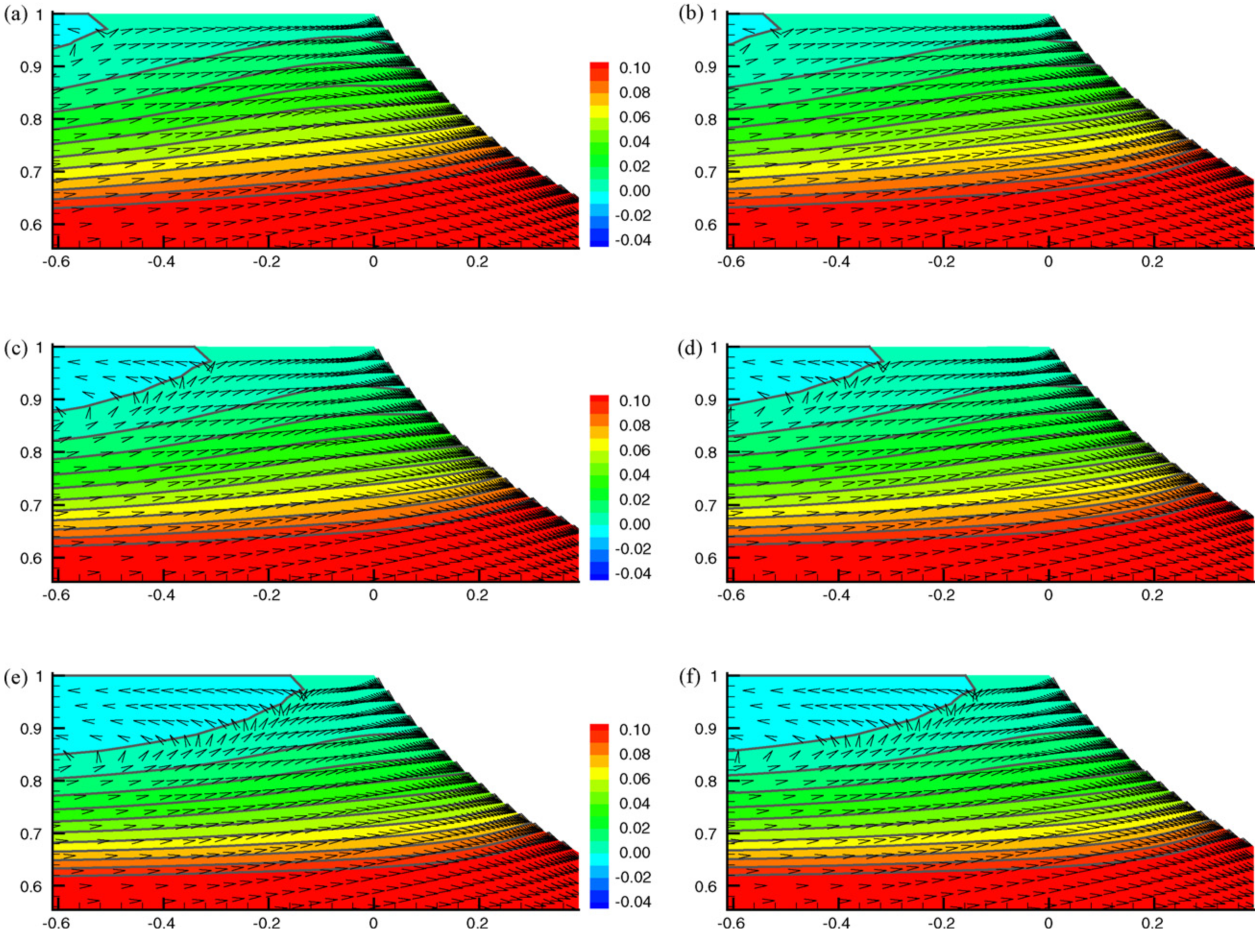

Fig. 18. Change in velocity profile by changing the viscosity ratio for the Oldroyd-B and FENE-P models. $Wi = 2.0$, $Ca = 0.1$, $Q = 0.3$, $b = 50$. (a) Oldroyd-B ($\beta = 0.25$), (b) FENE-P ($\beta = 0.25$), (c) Oldroyd-B ($\beta = 0.51$), (d) FENE-P ($\beta = 0.51$), (e) Oldroyd-B ($\beta = 0.75$) and (f) FENE-P ($\beta = 0.75$).

Fig. 16 shows the position of the stagnation point for an Oldroyd-B liquid as a function of Wi. The stagnation point is always on the free surface when $Wi \lesssim 1$, moves to the static contact line when $Wi \sim 1$ and on the die wall at higher Wi. As long as $(T_{nn} - T_{tt})$ is negative (see Fig. 12(b)), the stagnation point is on the free surface and it jumps to the die wall when $(T_{nn} - T_{tt})$ becomes positive. The strong extensional stresses arising from the viscoelastic nature of the fluid pulls the liquid out of the recirculation region and the recirculation zone shrinks as depicted in Fig. 17. For $Wi \gtrsim 1$, the recirculation region attached to the static contact line completely disappears.

The effect of the viscosity ratio and the constitutive model on the size of the recirculation zone is shown in Fig. 18. The recirculation is much smaller at $\beta = 0.25$ than at $\beta = 0.75$ because of the higher normal stress difference at smaller β val-

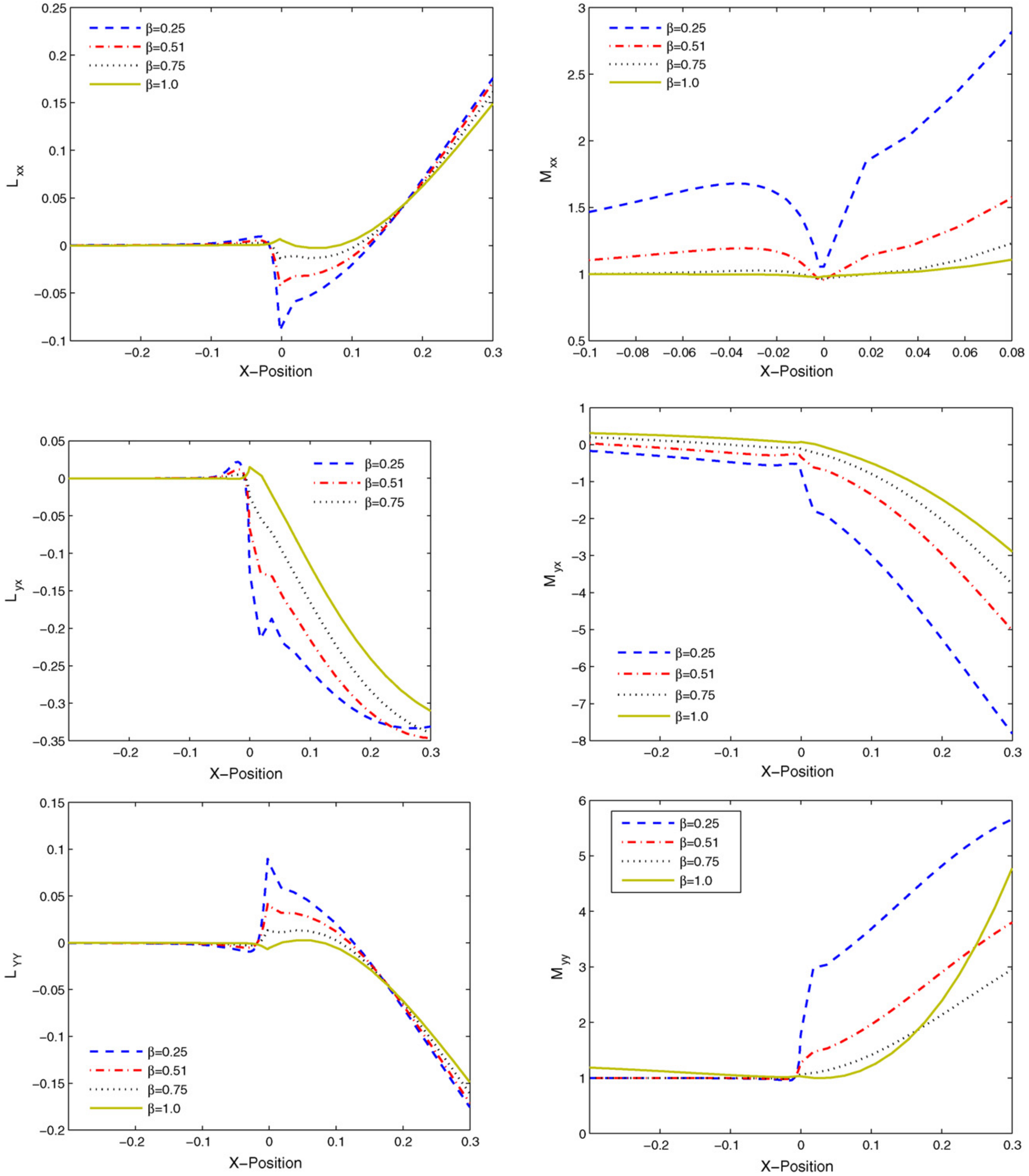

Fig. 19. Components of velocity gradient (left) and conformation tensor (right) for an Oldroyd-B fluid. X-axis shows the x-coordinate of the position while moving from the die wall to the free surface. $X = 0$ is static contact line. $Wi = 2.0$, $Ca = 0.1$, $Q = 0.3$.

ues. As shown in Fig. 18, the choice of constitutive model affects minimally the size of the recirculation. Both the Oldroyd-B and FENE-P models produce similar behavior with varying β values.

5.1.3. Effect of geometric singularity on mesh convergence

As a consequence of the shrinking recirculation zone, the geometric singularity that is present in slot coating flows is exposed in relatively strong flows. The geometric singularity arises due to the imposition of an inadequate boundary condition on the die wall and the free surface. While moving from the die wall to the free surface, the boundary condition changes from a no-slip boundary at the die wall to the shear-free condition on the free surface. Pasquali and Scriven [19] showed that for an ultra-dilute solution, the geometric singularity at the static contact line does not affect viscoelastic flow calculations when recirculation is present under the die (which occurs for $Q < 0.33$). An analysis of the flow field for an Oldroyd-B liquid near corners (formed by the intersection of a slip surface with either a no-slip or a shear-free boundary) by Salamon et al. [30] revealed that for dilute and ultra-dilute solutions both stress and flow fields have a singularity at the point of intersection of the free surface and the solid surface in the absence of the recirculation. They found that the strength of the singularity depends upon the dimensionless solvent viscosity (defined as β in this work) and in particular, for dilute solutions, the singularity in the rate-of-strain and elastic stress fields scale with $1/\beta$

Both the rate-of-strain and the conformation tensor for an Oldroyd-B fluid are plotted as a function of the X-position along the die wall and the free surface in Fig. 19. Clearly, the field variables become singular as the static contact line is approached; the singularity is much stronger for a smaller β value which is consistent with the findings of Salamon et al. [30]. The higher strength of the singularity in field variables and the requirement of refined meshes to capture higher normal stresses along the free surface explains why the conformation tensor loses its positive definiteness at a smaller Wi for decreasing values of β (Fig. 6).

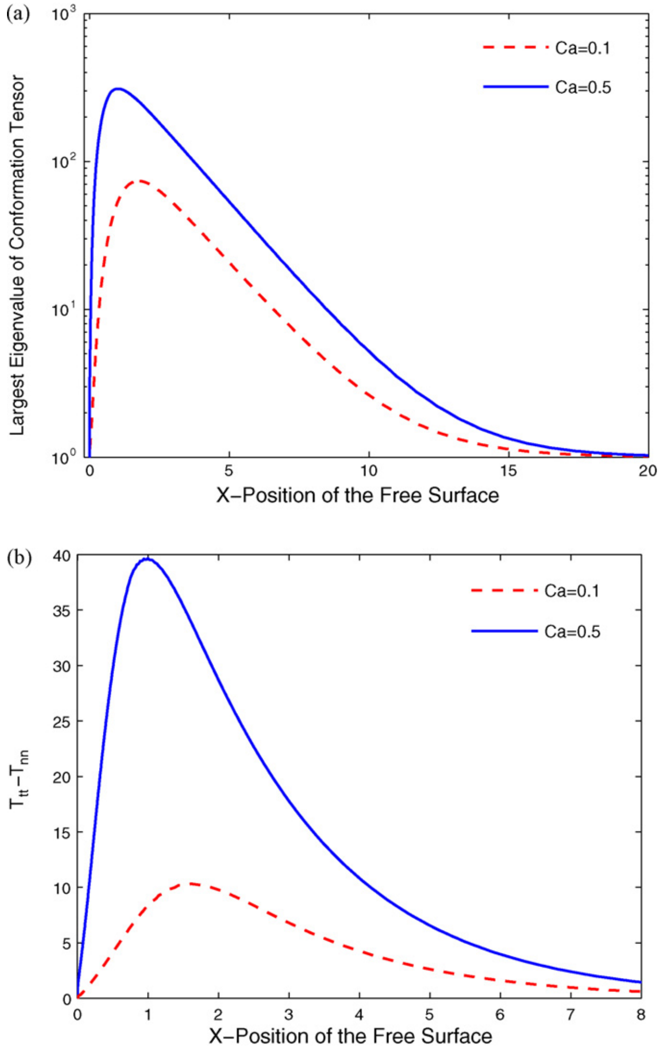

Fig. 20. Effect of Ca on the stretch and the normal stress difference for an Oldroyd-B fluid. $Wi = 2.0$, $Q = 0.3$, $\beta = 0.75$. (a) Largest eigenvalue of the conformation tensor along the free surface and (b) Hoop stress along the free surface.

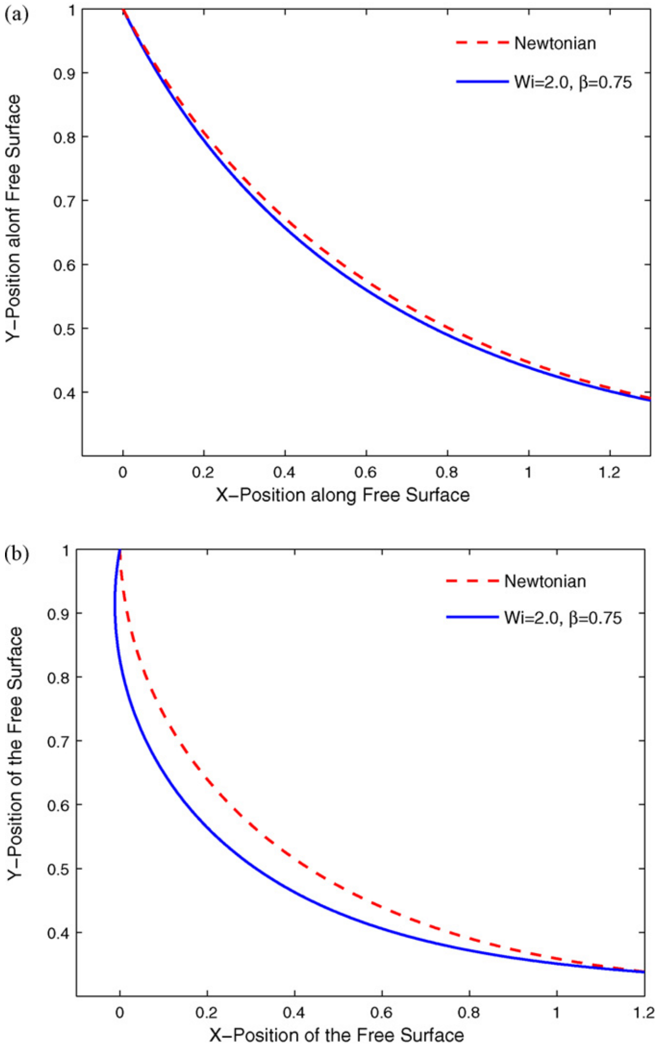

Fig. 21. Effect of Ca on free surface shape for an Oldyod-B fluid. Wi=2.0, $Q = 0.30$, $\beta = 0.75$. (a) $Ca = 0.1$ and (b) $Ca = 0.5$.

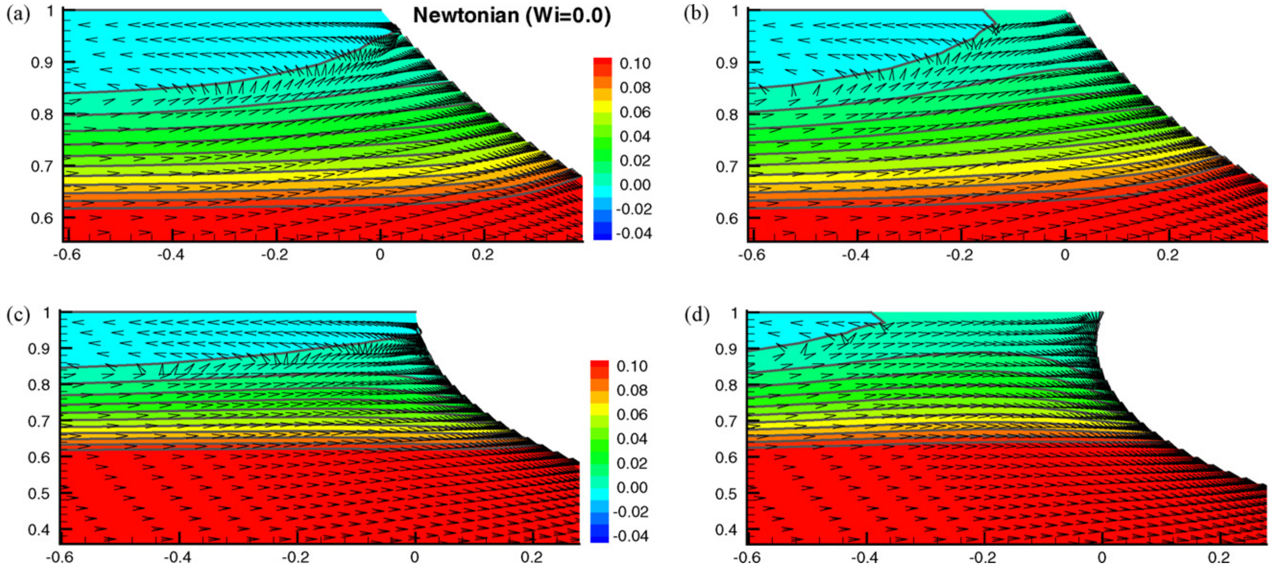

Fig. 22. Change in velocity profile by changing the Ca for an Oldroyd-B fluid. $Q = 0.3$. (a) Newtonian, $Ca = 0.1$, (b) $Wi = 2.0$, $\beta = 0.75$, $Ca = 0.1$, (c) Newtonian, $Ca = 0.5$ and (d) $Wi = 2.0$, $\beta = 0.75$, $Ca = 0.5$.

5.2. Effect of Ca

Here, we analyze the effect of Ca on microscopic and macroscopic flow properties at $Ca = 0.1$ and 0.5. As is well known for a Newtonian fluid, an increase in Ca causes the free surface to move into the die (meniscus invasion) [1–4,12]. The meniscus invasion causes the rate of strain or the velocity gradient to increase. Such higher rate of strain significantly affects the flow behavior of viscoelastic liquids. Fig. 20 shows the effect of Ca on the stretch of polymer molecules and on the normal stress difference along the streamlines on the free surface for an Oldroyd-B fluid. As expected, both the stretch and the stress are higher at $Ca = 0.5$ than at $Ca = 0.1$, because of the higher rate of strain.

The normal stress difference arising because of the fluid viscoelasticity contributes to the net pressure gradient at the free

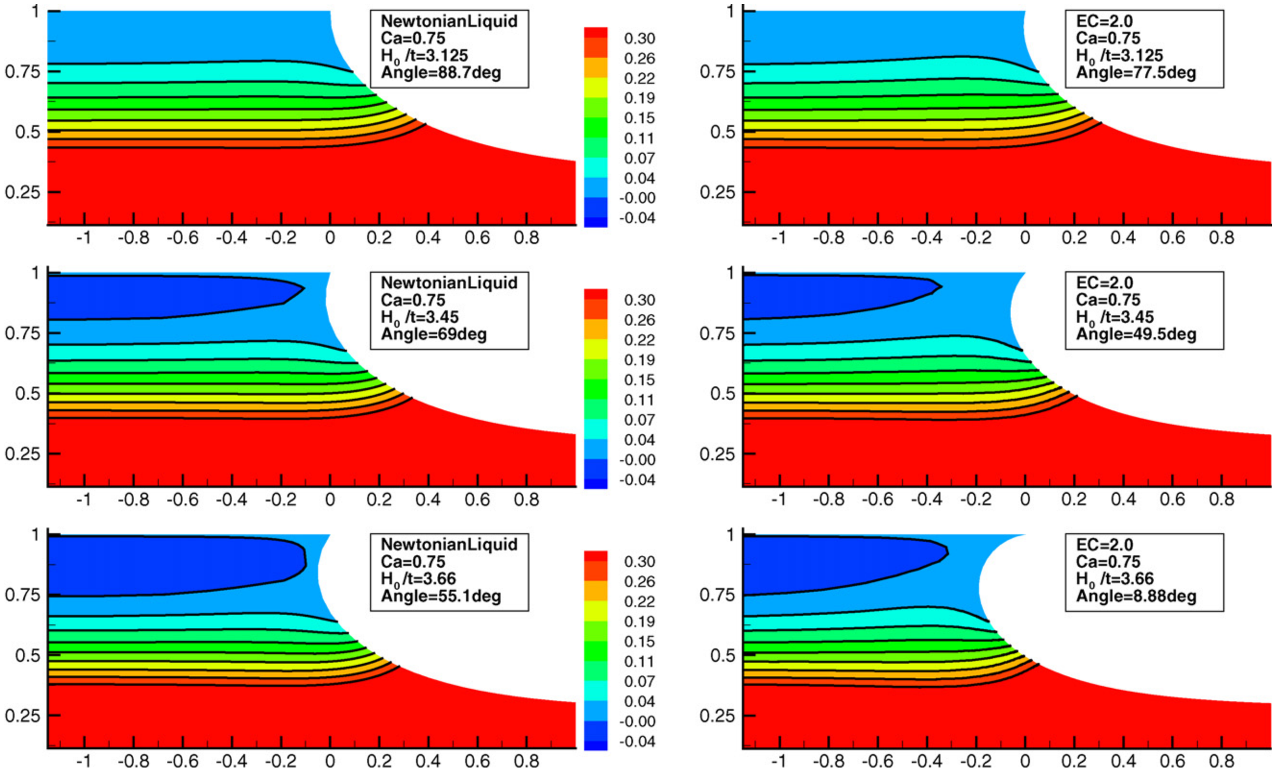

Fig. 23. Evolution of streamlines with the change in the gap to the coating thickness ratio (H_0/t). The Newtonian flow profile is on the left for $Ca = 0.75$ and flow profile for an Oldroyd-B liquid is on the right for $Ca = 0.75$, $Ec = 2.0$ and $\beta = 0.75$.

surface. In order to balance the increased pressure gradient due to viscoelasticity, the free surface must curve more than in a Newtonian liquid. The effect of viscoelasticity on meniscus invasion is displayed in Fig. 21 for two different Ca. While at smaller Ca the surface forces can balance the increased pressure difference without drastic changes in curvature (Fig. 21(a)), at high Ca (smaller surface tension), the free surface must curve more when the liquid is viscoelastic liquids compared to the Newtonian case (Fig. 21(b)).

Fig. 22 shows that in viscoelastic liquids the recirculation shrinks more at high Ca compared to that at lower Ca because the normal stress effect grows with Ca.

5.3. *Low flow limit in slot coating flows*

The viscoelasticity of the coating fluid affects the low-flow limit of slot coating. Fig. 23 shows the evolution of streamlines as a function of the gap to coating thickness ratio (H_0/t) for a Newtonian fluid and for an Oldroyd-B liquid at $Ca = 0.75$, $Ec = 2.0$ and $\beta = 0.75$. As the ratio H_0/t increases, the free surface becomes more curved and the contact angle (θ) between the free surface and the die wall diminishes. Fig. 23 shows that viscoelasticity leads to smaller contact angle compared to the Newtonian fluids; this limits the minimum coating thickness that can be coated at a given flow rate. However, the extent of this reduction depends on Ca at a given β and Ec (Fig. 24 (a)). For a given H_0/t, β, and Ec, the static contact angle θ decreases as Ca increases for both Newtonian and Oldroyd-B liquids [4,12,23,33]. At low Ca surface tension forces are strong enough that there is little difference between Newtonian and viscoelastic liquids with Ec up to ≈ 2. As the normal stress difference grows with Ca (lower surface forces), the free surface curves more at high Ca. Higher Ec or lower β yields higher normal stresses at a given Ca and the ratio H_0/t; the computed contact angle decreases more rapidly. The effect of β is displayed in Fig. 24(b).

Fig. 24(c) shows the effect of the finite extensibility of the polymer molecules on the contact angle. For the FENE-P model the normal stresses at the free surface are smaller (due to shear thinning) than the stresses predicted by the Olydroyd-B model for $b = 50$. Hence, the change in contact angle for the FENE-P model is less steep compared to the change in contact angle for the Oldroyd-B model.

Romero et al. [23] established that the critical conditions for the low-flow limit obtained by solving only the downstream section of a slot coater are virtually the same as those predicted for the full slot coater [12,23] for $Ca \approx 1$ and inertialess flows. As only the downstream section of the slot coater has been analyzed in this work, the low-flow limit computed here is limited to $0.1 \lesssim Ca \lesssim 1$ and inertialess flows.

Following Ref. [23], the onset of the low-flow limit at a given Ca is determined by computing the ratio H_0/t at which the static contact angle falls below 20° as shown in Fig. 24. Fig. 25 display the critical conditions for the low-flow limit predicted using the Oldroyd-B and FENE-P models. For the Oldroyd-B model, the onset of the low-flow limit occurs at a lower gap to coating thickness ratio compared to a Newtonian fluid for all values

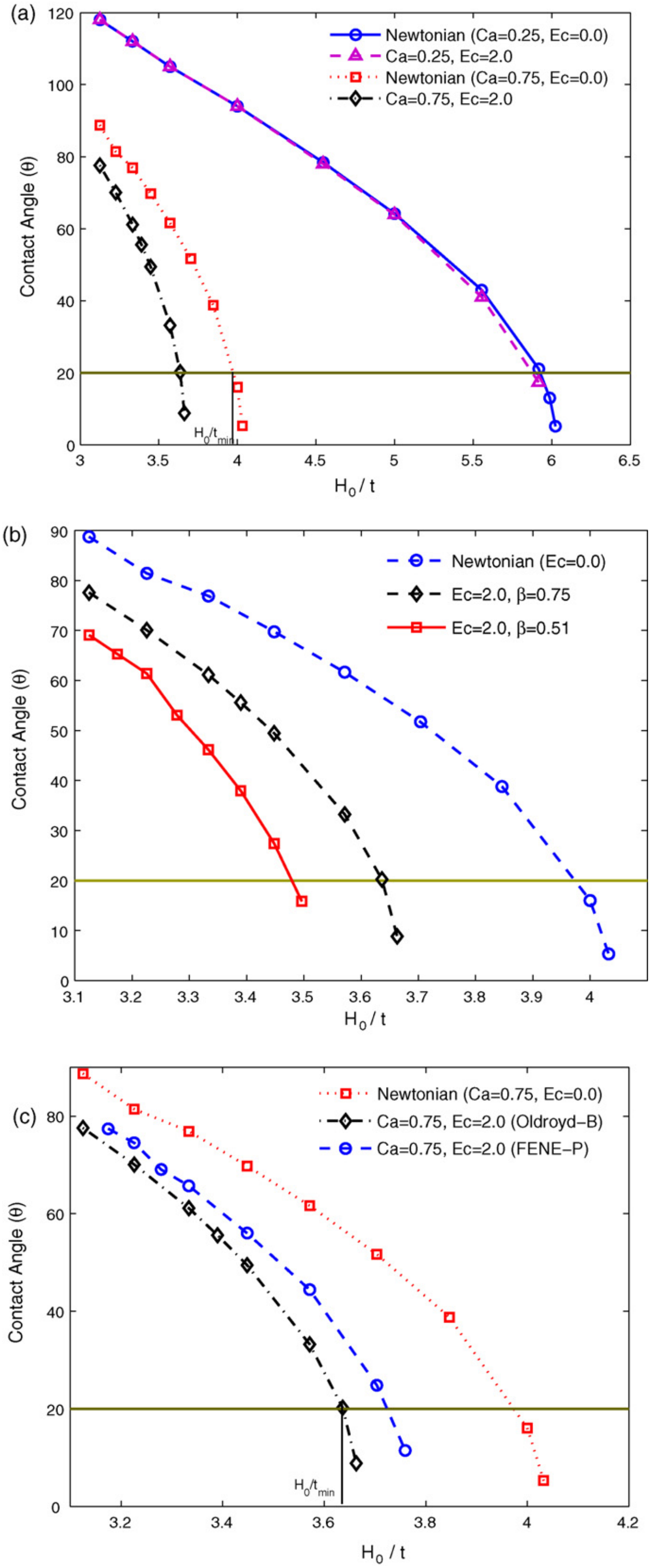

Fig. 24. Change in the contact angle with the change in the gap to coating thickness ratio (H_0/t). $H_0/t_{\min}$ shown in the figure is used to predict the low-flow limit.(a) Effect of Ca for Newtonian and Oldroyd-B fluids ($\beta = 0.75$), (b) effect of the viscosity ratio β for an Oldroyd-B fluid ($Ca = 0.75$) and (c) change in contact angle for different constitutive models ($\beta = 0.75$, $b = 50$).

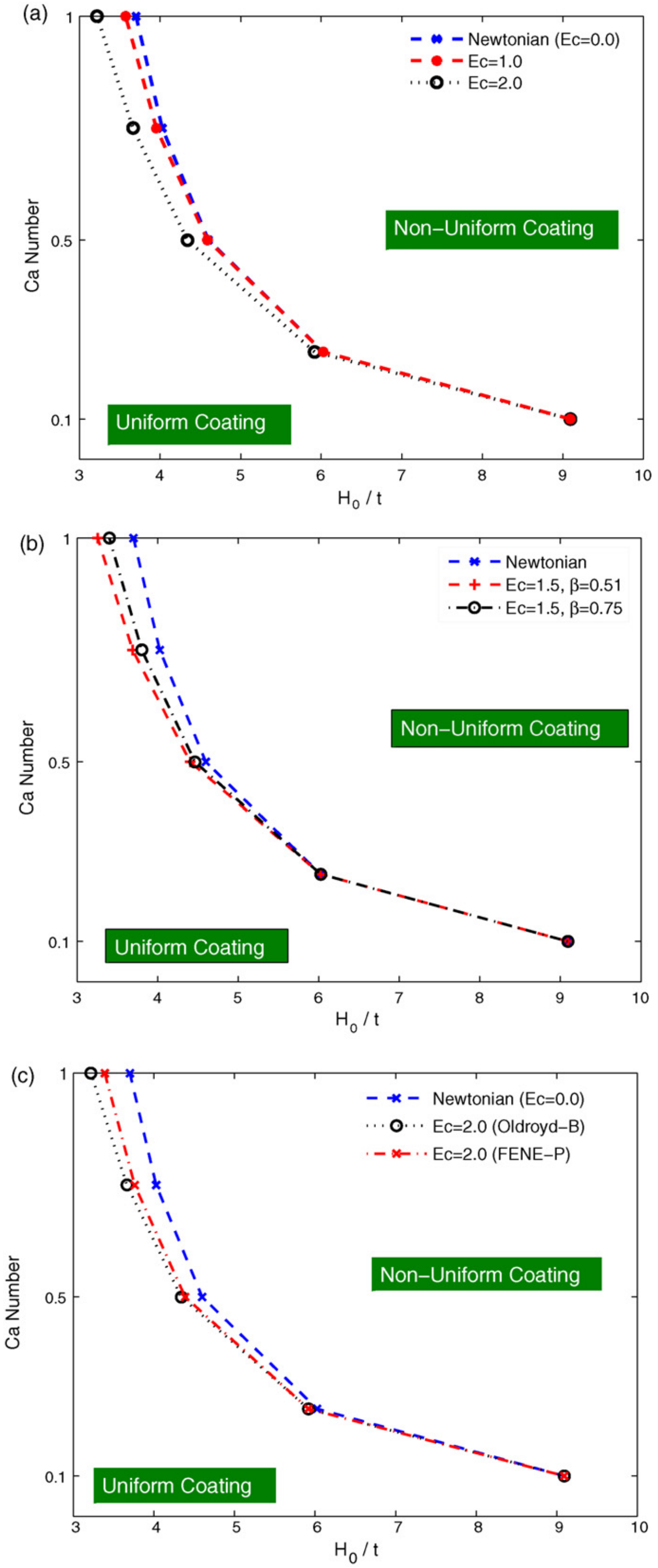

Fig. 25. Effect of viscoelasticy on the size of coating window. (a) Effect of *Ec* for an Oldroyd-B fluid ($\beta = 0.75$), (b) effect of viscosity ratio β for an Oldroyd-B fluid and (c) coating window for different constitutive models ($\beta = 0.75$, $b = 50$).

of *Ec* and β considered (Fig. 25(a) and (b)). The minimum film thickness that can be coated increases as the liquid becomes more viscoelastic. A reduction in the size of the coating window has been reported earlier by Romero et al. [23] both experimentally and theoretically.

Rheological properties of liquids (e.g., shear thinning) strongly the affects size of the coating window. Fig. 25(c) compares the critical conditions for different constitutive models. As predicted, for the FENE-P model with $b = 50$ the onset of the low flow limit occurs at a higher gap to coating thickness ratio compared to the Oldroyd-B model because of smaller normal stresses.

6. Conclusion

In this paper, the flow behavior of Oldroyd-B and FENE-P liquids in the downstream section of slot coating flow has been investigated. The DEVSS-TG finite element method coupled with an elliptic mesh generation scheme was used to solve the transport and mesh equations. The flow behavior of dilute polymer solutions differs dramatically from that of ultra-dilute solutions. In ultra-dilute solutions, the maximum *Wi* that can be achieved before the conformation tensor becomes negative definite depends strongly on mesh refinement and constitutive model. In contrast, the maximum attainable *Wi* is nearly independent of mesh and constitutive model in dilute solutions.

The flow transitions between two regimes at a critical Weissenberg number, Wi_{L}^{*}. Below Wi_{L}^{*}, polymer molecules are predominantly stretched in the shear flow at the web; the rate of stretching of molecules is independent of the viscosity ratio. Beyond Wi_{L}^{*}, polymer molecules are chiefly stretched in the extensional flow at the free surface; the rate of stretching decreases with viscosity ratio. Wi_{L}^{*} is nearly unaffected by the choice of constitutive equation.

In dilute polymer solutions, the position of the smallest eigenvalue of the conformation tensor abruptly moves to the static contact line at high *Wi* just before numerical simulations fail. On the other hand, the position of the smallest eigenvalue always remains on the free surface in ultra-dilute solutions. This important observation suggests that the mode of failure for dilute polymer solutions is due to the artificial geometric singularity at the static contact line; for ultra-dilute solutions, it occurs because mesh can not capture steep stress boundary layers close to the free surface.

In dilute solutions, the high normal stresses at the free surface pull the liquid away from the recirculation region present in a Newtonian flow under the web. As a result, the recirculation zone shrinks, and flow close to the static contact line becomes stronger. The stagnation point moves from the free surface to the die wall and the normal stress difference close to the static contact line becomes positive. Consequently, various field variables, such as the velocity gradient and conformation tensor, become singular.

We have also investigated the effects of viscoelasticity and viscosity ratio on the low-flow limit of slot coating flows. We find that for viscoelastic liquids, the minimum coating thickness is higher than the coating thickness for Newtonian liquids, i.e., the coating window of a viscoelastic fluid is smaller than that of a Newtonian fluid of equal zero-shear viscosity.

Acknowledgements

We thank Pradeep P. Bhat and P. Sunthar for useful discussions. This work has been supported by the Cooperative Research Center for Functional Communication Surfaces, Australia, Monash Research Graduate School, the National Science Foundation (CTS-CAREER- 0134389 and CTS-ITR-0312764) and by gifts from ExxonMobil and 3M Corporation. The authors would like to thank the Australian Partnership for Advanced Computing (APAC) (Canberra, Australia), Victorian Partnership for Advanced Computing (VPAC) (Melbourne, Australia), the Rice Terascale Cluster funded by NSF (EIA-0216467), Intel, and Hewlett-Packard, and the Rice Cray XD1 Research Cluster funded by NSF (CNS-0421109), AMD, and Cray for the allocation of computing time on their supercomputing facilities.

References

[1] S.F. Kistler, L.E. Scriven, Coating flow theory by finite element and asymptotic analysis of the Navier–Stokes system, Int. J. Numer. Methods Fluid. 4 (1984) 207–229.

[2] K.J. Ruschak, Limiting flows in pre-metered coating device, Chem. Eng. Sci. 31 (1976) 1057–1060.

[3] W.J. Silliman, L.E. Scriven, Separating flow near a static contact line-slip at a wall and shape of a free-surface, J. Comp. Phys. 34 (1980) 287–313.

[4] H. Saito, L.E. Scriven, Study of coating flow by the finite element method, J. Comp. Phys. 42 (1981) 53–76.

[5] K.N. Christodoulou, L.E. Scriven, Discretization of free surface flows and other moving boundary problems, J. Comp. Phys. 99 (1992) 39–55.

[6] M.S. Carvalho, L.E. Scriven, Flows in forward deformable roll coating gaps: comparison between spring and plane strain model of roll cover, J. Comp. Phys. 138 (1997) 449–479.

[7] M.S. Carvalho, L.E. Scriven, Deformable roll coating flows: steady state and linear perturbation analysis, J. Fluid Mech. 339 (1997) 143–172.

[8] M.S. Carvalho, L.E. Scriven, Three-dimensional stability analysis of free surface flows: application to forward deformable roll coating, J. Comp. Phys. 151 (1999) 534–562.

[9] L. Sartor, Slot Coating: Fluid Mechanics and Die Design, PhD thesis, University of Minnesota, Minneapolis, MN, 1990 (available from UMI, Ann Arbor, MI, order number 9109372).

[10] I.D. Gates, Slot Coating Flows: Feasibility, Quality, PhD thesis, University of Minnesota, Minneapolis, MN, 1999 (available from UMI, Ann Arbor, MI, order number 9946975).

[11] L.C. Musson, Two-layer slot coating, PhD thesis, University of Minnesota, Minneapolis, MN, 2001 (available from UMI, Ann Arbor, MI, order number 3008715).

[12] M.S. Carvalho, H.S. Kheshgi, Low-flow limit in slot coating: theory and experiments, AIChE J. 1917 (2000) 46.

[13] J.R.A. Pearson, The stability of viscous flows under rollers and spreaders, J. Fluid Mech. 7 (1960) 481–500.

[14] E. Pitts, J. Greiller, The flow of thin liquid films between rollers, J. Fluid Mech. 11 (1961) 33–50.

[15] C.C. Mill, G.R. South, Formation of ribs on rotating rollers, J. Fluid Mech. 28 (1967) 523–529.

[16] M. Savage, Mathematical model for the onset of ribbing, AIChE J. 30 (1984) 999–1002.

[17] D.J. Coyle, C.W. Macosko, L.E. Scriven, Stability of symmetrical film splitting between conter-rotating rollers, J. Fluid Mech. 216 (1990) 437–458.

[18] J. Greener, T. Sullivan, B. Turner, S. Middleman, Ribbing instabilities of a two-roller coater: Newtonian fluids, Chem. Eng. Commun. 5 (1980) 73–83.

[19] M. Pasquali, L.E. Scriven, Free surface flows of polymer solutions with models based on the conformation tensor: computational method and benchmark problems, J. Non-Newtonian Fluid Mech. 108 (2002) 363–409.

[20] A.G. Lee, E.S.G. Shaqfeh, B. Khomami, A study of viscoelastic free surface flows by finite element method: Hele–Shaw and slot coating flows, J. Non-Newtonian Fluid Mech. 108 (2002) 327–362.

[21] G. Bhatara, E.S.G. Shaqfeh, B. Khomami, Influence of viscoelasticity on the interfacial dynamics of air displacing fluid flows—a computational study, J. Non-Newtonian Fluid Mech. 122 (2004) 313–332.

[22] G. Bhatara, E.S.G. Shaqfeh, B. Khomami, The influence of polymer concentration and chain architecture on free surface displacement flows of polymeric fluids, J. Rheol. 49 (2005) 929–962.

[23] O.J. Romero, W.J. Suszynski, L.E. Scriven, M.S. Carvalho, Low-flow limit in slot coating of dilute solutions of high molecular weight polymer, J. Non-Newtonian Fluid Mech. 118 (2004) 137–156.

[24] G.A. Zevallos, M.S. Carvalho, M. Pasquali, Forward roll coating flows of viscoelastic liquids, J. Non-Newtonian Fluid Mech. 130 (2005) 96–109.

[25] M. Bajaj, P.P. Bhat, J.R. Prakash, M. Pasquali, Multiscale simulation of viscoelastic free surface flows, J. Non-Newtonian Fluid Mech. 140 (2006) 87–107.

[26] P.A. Sackinger, P.R. Schunk, R.R. Rao, A Newton-Raphson pseudo-solid domain mapping technique for free and moving boundary problems: a finite element implementation, J. Comp. Phys. 125 (1996) 83–103.

[27] V.F. deAlmeida, Domain deformation mapping: application to variational mesh generation, SIAM J. Sci. Comput. 20 (1999) 1252–1275.

[28] T.R. Salamon, D.E. Bornside, R.C. Armstrong, R.A. Brown, The role of surface tension in the dominant balance in the die swell singularity, Phys. Fluids 7 (1995) 2328–2344.

[29] T.R. Salamon, D.E. Bornside, R.C. Armstrong, R.A. Brown, Local similarity solutions in the presence of a slip boundary condition, Phys. Fluids 9 (1997) 1235–1247.

[30] T.R. Salamon, D.E. Bornside, R.C. Armstrong, R.A. Brown, Local similarity solutions for the stress field of an Oldroyd-B fluid in the partial-slip/slip flow, Phys. Fluids 9 (1997) 2191–2209.

[31] M.D. Graham, Interfacial hoop stress and instability of viscoelastic free surface flows, Phys. Fluids 15 (2003) 1702–1710.

[32] B.G. Higgins, L.E. Scriven, Ribbing instabilities of a two-roller coater: Newtonian fluids, Chem. Eng. Sci. 35 (1980) 459–466.

[33] O.J. Romero, L.E. Scriven, M.S. Carvalho, Slot coating of mildly viscoelastic liquids, J. Non-Newtonian Fluid Mech. 138 (2006) 63–214.

[34] L. Landau, B. Levich, Dragging of a liquid by a moving plate, Acta Physicochim. 17 (1942) 42.

[35] P.R. Schunk, L.E. Scriven, Constitutive equations for modeling mixed extension and shear in polymer solution processing, J. Rheol. 34 (1990) 1085–1119.

[36] A.N. Beris, B.J. Edwards, Thermodynamics of Flowing Systems with Internal Microstructure, 1st ed., Oxford University Press, Oxford, 1994.

[37] R.J.J. Jongschaap, K.H. deHaas, C.A.J. Damen, A generic matrix representation of configuration tensor rheological models, J. Rheol. 38 (1994) 769–796.

[38] M. Grmela, P.J. Carreau, Conformation tensor rheological models, J. Non-Newtonian Fluid Mech. 23 (1987) 271–294.

[39] M. Pasquali, L.E. Scriven, Theoretical modelling of microstructured liquids: a simple thermodynamic approach, J. Non-Newtonian Fluid Mech. 120 (2004) 101–135.

[40] J.M. de Santos, Two-phase Cocurrent Downflow Through Constricted Passages, PhD thesis, University of Minnesota, Minneapolis, MN, 1991 (available from UMI, Ann Arbor, MI, order number 9119386).

[41] J.C. Slattery, Interfacial Transport Phenomena, Springer-Verlag, 1990.

[42] X. Xie, M. Pasquali, A new, convenient way of imposing open-flow boundary conditions in two- and three-dimensinoal viscoelastic flows, J. Non-Newtonian Fluid Mech. 122 (2004) 159–176.

[43] R. Guénette, M. Fortin, A new finite element method for computing viscoelastic flows, J. Non-Newtonian Fluid Mech. 60 (1995) 27–52.

[44] M.J. Szady, T.R. Salamon, A.W. Liu, R.C. Armstrong, R.A. Brown, A new mixed finite element method for viscoelastic flows governed by differential constitutive equations, J. Non-Newtonian Fluid Mech. 59 (1995) 215–243.